

**COMPARISON OF 2 μm Ho and 10 μm CO₂ LIDAR FOR
ATMOSPHERIC BACKSCATTER AND DOPPLER
WINDSHEAR DETECTION**

*Langley
GRANT*

10-47-CR

53078

P48

**PROGRESS REPORT
NASA GRANT NAG-1-1104**

For Period: March, 1990 - October, 1991

submitted to:

Dr. Norm Barnes
Flight Electronics Division
NASA/Langley Research Center
Hampton, VA 23665-5225
Ph(804) 864-1630

by

Prof. Dennis Killinger
Department of Physics
University of South Florida
Tampa, Florida 33620
Ph(813) 974-3995

NOVEMBER 22, 1991

(NASA-CR-189471) COMPARISON OF 2 MICRON Ho
AND 10 MICRON CO₂ LIDAR FOR ATMOSPHERIC
BACKSCATTER AND DOPPLER WINDSHEAR DETECTION
Progress Report, Mar. 1990 - Oct. 1991
(University of South Florida) 48 p CSCL 048 G3/47

N92-13523

Unclass
0053078

Table of Contents

	Page
1.0 Introduction	2
1.1 Overview of Program Tasks	2
2. Specific Progress Items	3
2.1 Tunable Ho DIAL/Lidar	3
2.2 Atmos. Turbulence Meas./Detector Array	9
2.3 Diurnal Meas. of C_n^2 at KSC	12
2.4 Joint Development of Ho Laser	12
3. Anticipated Future Program Tasks	16
4. References	18
5. Appendices (Reprints of Journal Articles)	18

COMPARISON OF 2 μm Ho and 10 μm CO₂ LIDAR FOR ATMOSPHERIC BACKSCATTER AND DOPPLER WINDSHEAR DETECTION

**PROGRESS REPORT
NASA GRANT NAG-1-1104**

For Period: March, 1990 - October, 1991

1.0 INTRODUCTION:

This report summarizes progress made during the past year and a half on a research program funded by NASA/LaRC and conducted by Prof. D. Killinger's Lidar Research Group at the University of South Florida. This research has been directed toward the development of eye-safe, solid-state Lidar systems, with an emphasis on Coherent Doppler Lidar for Atmospheric Wind Measurements. Details of the Tasks and progress made are in the following sections of this report. The most important details of the progress made are presented in the following sections, along with supporting related documentation (reprints of scientific journal articles) which are enclosed in the Appendix of this report.

1.1 OVERVIEW OF PROGRAM TASKS:

The original program had Tasks to develop the Ho Lidar system, compare its performance with a CO₂ Lidar system for the detection of atmospheric backscatter, and develop (with NASA/LaRC) a coherent Doppler Ho Lidar system for potential windshear detection. This program was divided into two phases. Phase I (Task 1) involved the measurement of atmospheric backscatter coefficient, β , for the Ho and CO₂ Lidar systems. During this time, it was anticipated that NASA/LaRC would be finishing the development of a single-frequency Ho laser source. Phase II (Task 2) involves the

cooperative development of a coherent Doppler Ho Lidar using the Ho laser developed at LaRC and the Ho Lidar system at USF.

Task 1, involving the measurement of the backscatter coefficient of the atmosphere, β , has been completed, and Task 2, involving the development of a Ho Coherent Lidar, has been initiated. A slight modification to the original program was made to better accommodate the schedule of the completion of the single-frequency Ho laser and to allow involvement in NASA/Lockheed atmospheric wind measurements during a recent Shuttle Launch at KSC. As such, an additional subtask involving measurements of atmospheric refractive turbulence was made in support of another NASA Lidar program, instead of the continued CO₂ Lidar studies.

2.0 SPECIFIC PROGRESS ITEMS:

Significant progress has been made already under this program. We have recently demonstrated for the first time (1) the tuning of the Ho laser over a water vapor absorption line in the atmosphere, (2) measured simultaneously the range-resolved Lidar mapping of atmospheric aerosols and water vapor concentration, (3) measured the temporal and range-resolved attenuation and backscatter coefficient of the atmosphere, (4) measured the temporal variation in atmospheric refractive turbulence and performed related Coherent Lidar performance calculations, and (5) made initial progress in the joint development of a single-frequency, high power Ho Laser/Coherent Lidar system. Details of these items are presented in the following sections.

2.1 Tunable Ho DIAL/Lidar Atmospheric Measurements

The direct-detection 2.1 μm Ho:YSGG Lidar system was developed and used to measure the range-resolved backscatter coefficient of the atmosphere. In addition, through the use of intracavity tuning etalons, the wavelength of the Ho laser was tuned across an absorption line of water vapor in the atmosphere; range-resolved

Lidar measurements of atmospheric water vapor were also demonstrated.

Figure 1 shows initial Lidar/DIAL Ho measurements of the atmospheric backscatter and water vapor density. As can be seen, even with a low power 7 mJ/pulse Ho laser, range resolved measurements at ranges of several kilometers is easily obtainable. Details of the development of the Q-switched Ho laser source are given in the Appendix (reprint of Journal article), and details concerning the initial water vapor measurements of the atmosphere are also given in the Appendix.

An improved version of the Ho Lidar system has recently been completed and enhanced performance of the system has also been demonstrated. In this case, the Ho laser was upgraded to include better output coupling mirrors, an A/O Q-switch, and low loss transmitting mirrors. The output parameters of the Ho laser was 25 mJ/pulse and a 90 ns pulselength. Figure 2 shows a schematic of the improved Ho direct-detection Lidar system. Range-resolved measurements have been obtained out to a range of 3 km. Measurements of the temporal variation of the atmospheric attenuation coefficient, α , and the backscatter coefficient, β , were made, in order to calibrate the system sensitivity and to better understand the important Lidar atmospheric parameters for a 2.1 μm Ho Lidar. Figure 3 shows our Lidar data obtained over a 24 hour period. The "error bars" do not represent the accuracy of the measurement, but show the range-resolved variability in the value of α or β measured along the line-of-sight of the Lidar beam; the range resolution of the system was about 100m.

Of interest is the data shown in Fig. 4, which presents the ratio of α/β . This ratio shows a large change during the day and seems to indicate that the composition of the backscatter aerosols is changing from predominately water based aerosols to dry-particulate based aerosols. The ratio of α/β on the order of 10 to 100 tends to indicate water vapor aerosol formation, and a ratio on the order of 100 to 500 tends to indicate dry or dust aerosol composition. Further

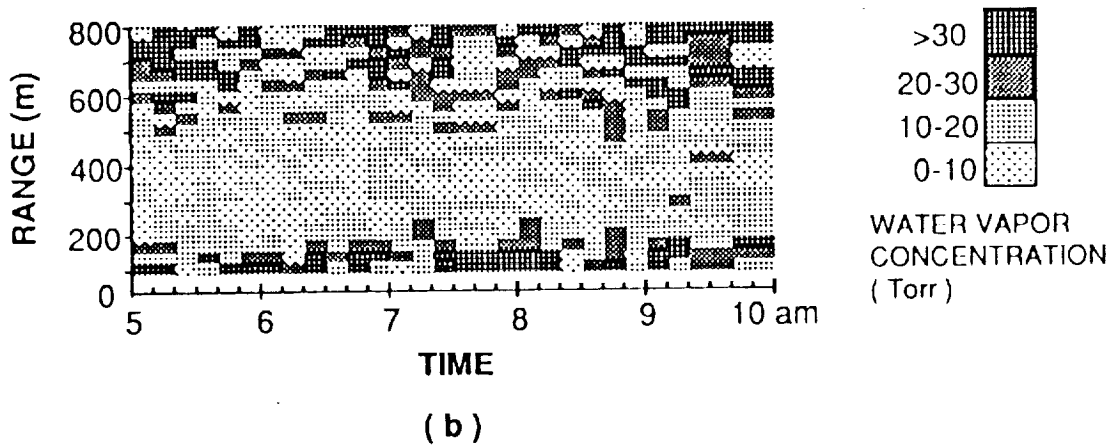
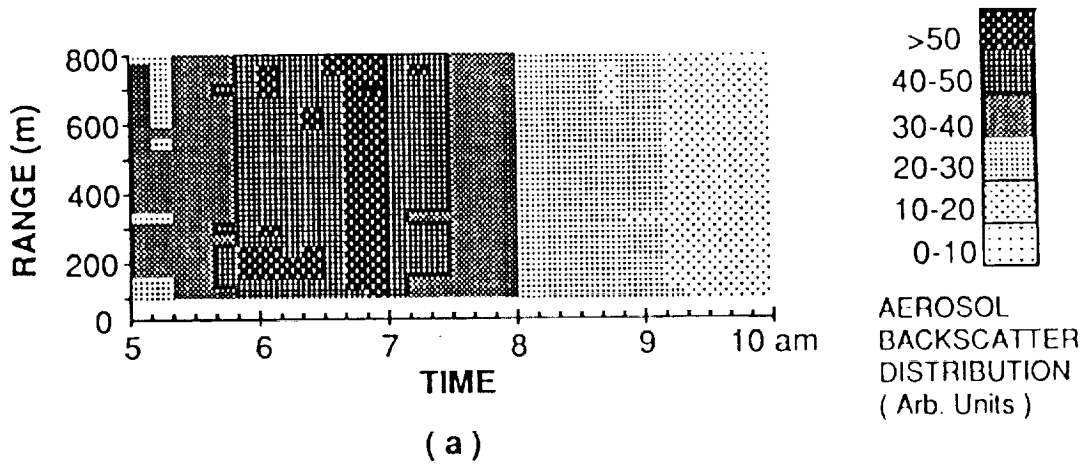


Fig. 1 Ho lidar/DIAL measurements of the temporal variation of (a) the atmospheric aerosol backscattering profile and (b) the atmospheric water-vapor concentration profile. The lidar was pointed at approximately a +2° elevation angle.

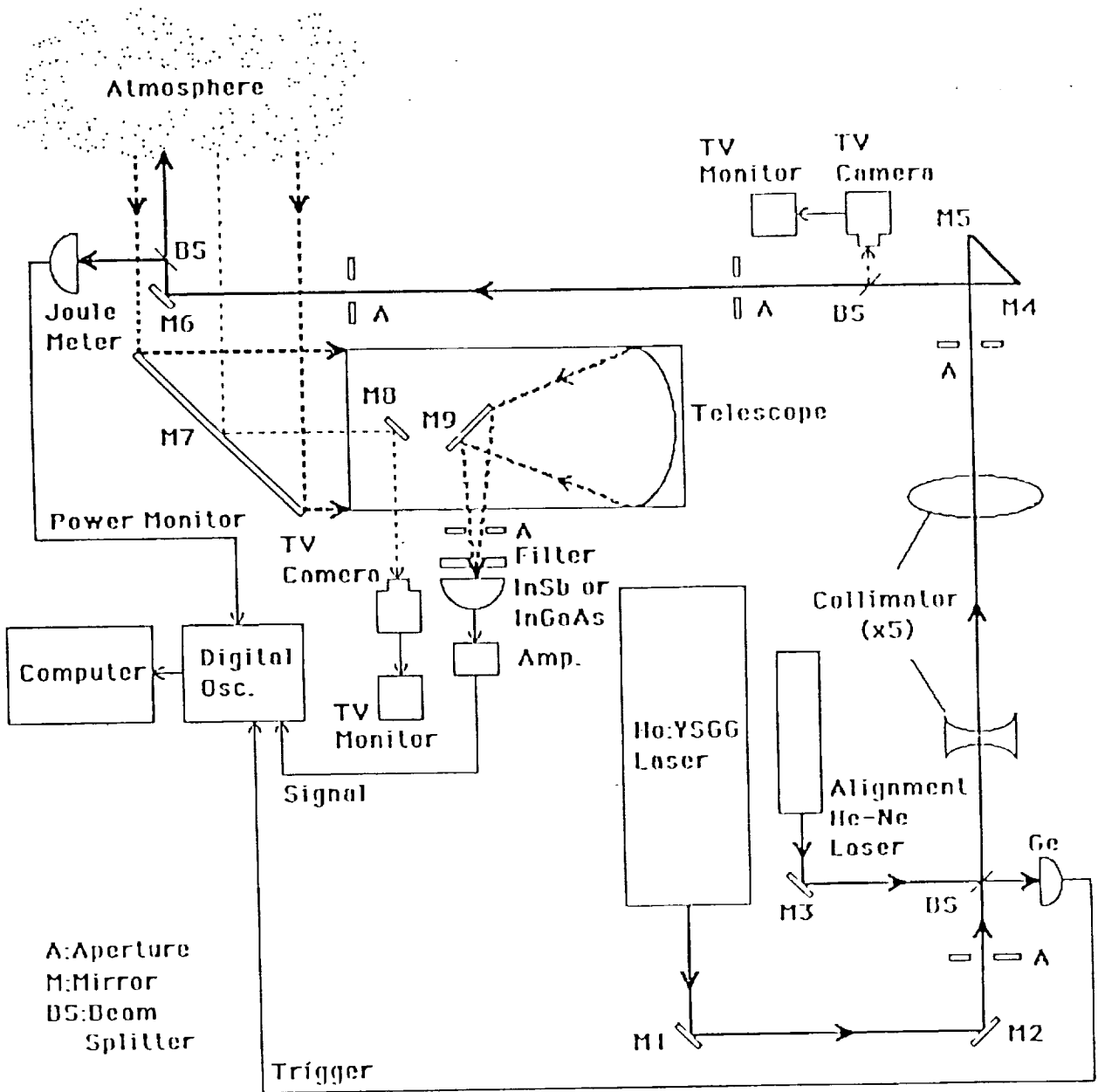


Fig. 2 Schematic of Q-switched Ho:YSGG DIAL/Lidar system

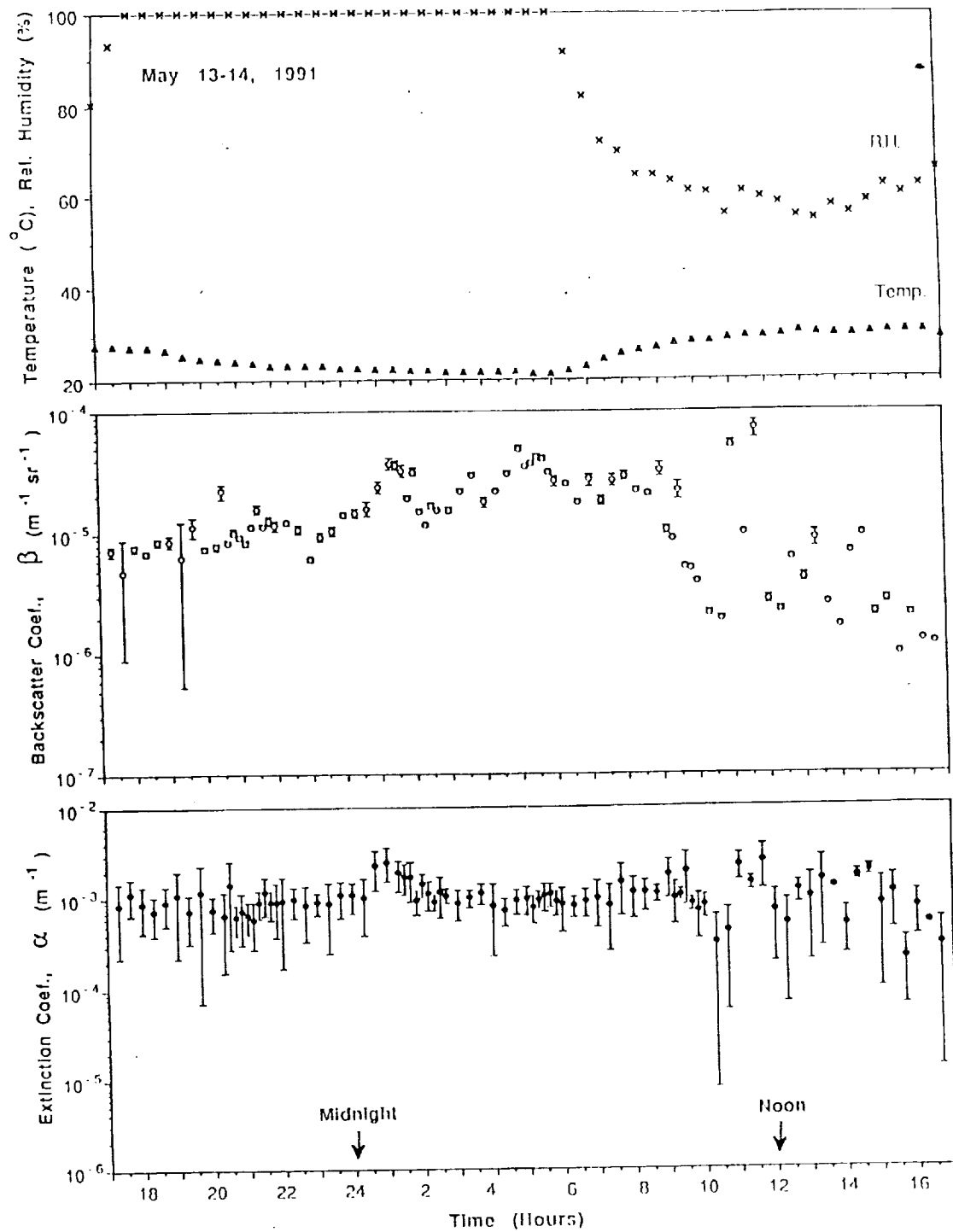


Fig. 3 Diurnal and Range-resolved variation in Ho Lidar measurements of atmospheric extinction coefficient and backscatter coefficient.

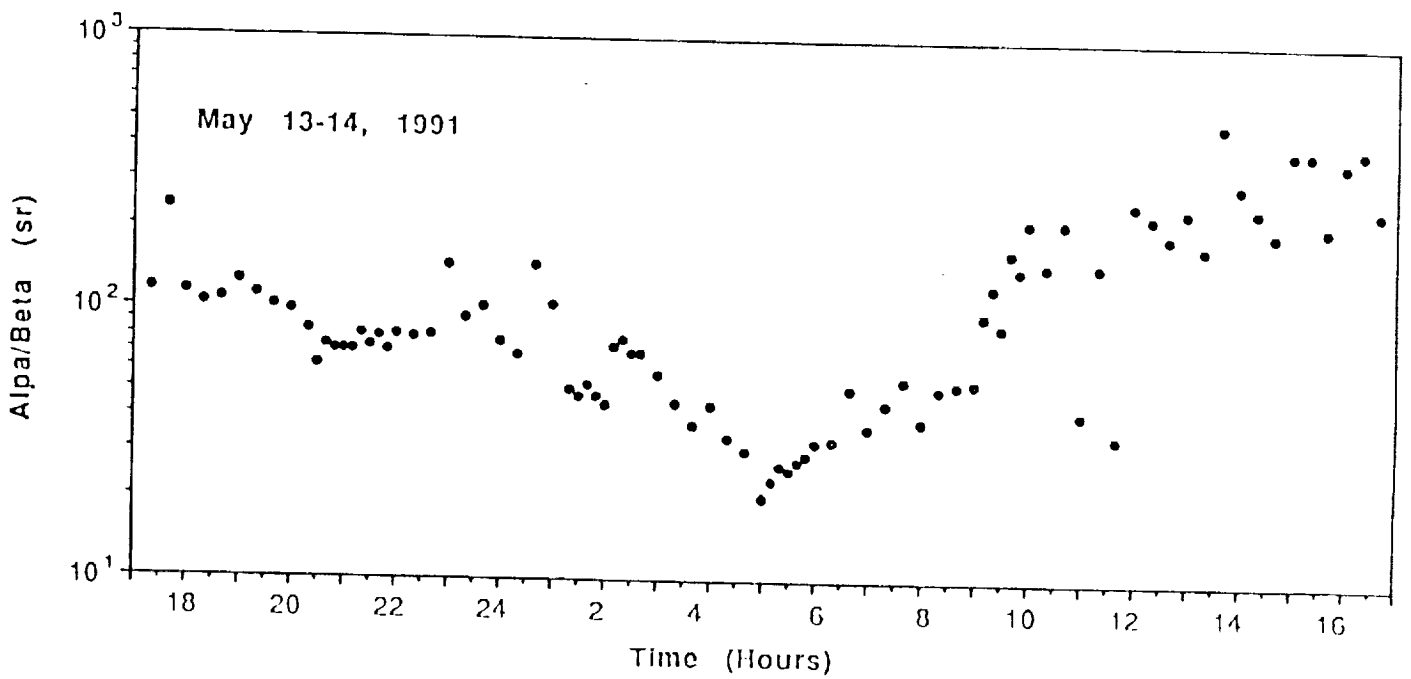


Fig. 4 Ho Lidar measurements of α/β as a function of time

measurements are being planned to better quantify these results; a journal paper has been submitted on these results.

2.2 Atmospheric Turbulence Measurements and Detector Arrays

Early work which we performed in 1989 showed experimentally for the first time that atmospheric refractive turbulence would severely hurt the performance of some Coherent Lidar systems operating in the near to mid-IR; this work was part of another study which investigated a 1 μm Coherent Doppler Lidar for rocket plume measurements. The results of these studies were applied to the case of a 2.1 μm Ho Lidar for atmospheric wind sensing. The pertinent results are shown in Fig. 5 which gives the predicted maximum Lidar telescope size as a function of wavelength, range, slant path angle, and turbulence level; here WN (Winter Night) refers to a turbulence level of $C_n^2 = 2 \times 10^{-12} \text{ m}^{-2/3}$, and SD(Summer Day) to $C_n^2 = 1 \times 10^{-13} \text{ m}^{-2/3}$. As can be seen, a Ho Coherent Lidar may be limited to telescope apertures on the order of 20 - 50 cm under high turbulence levels and horizontal (ground based) operation. Figure 6 shows similar data for a 2 μm Ho Coherent Lidar operating from space. As can be seen, rather large telescopes are usable. Details of these studies are presented in the Appendix and in another journal article which has been submitted for publication.

It should be noted that the reduced Coherent Lidar signal due to atmospheric refractive turbulence can be overcome by use of a multi-element heterodyne detector array. We have recently shown that the Lidar S/N can be improved by a factor of N^2 through use of a $N \times N$ heterodyne detector array.¹ We plan to investigate the use of such an array for the enhancement of the Ho Coherent Lidar S/N, and the use of the array for target tracking and "Lag Angle" compensation.

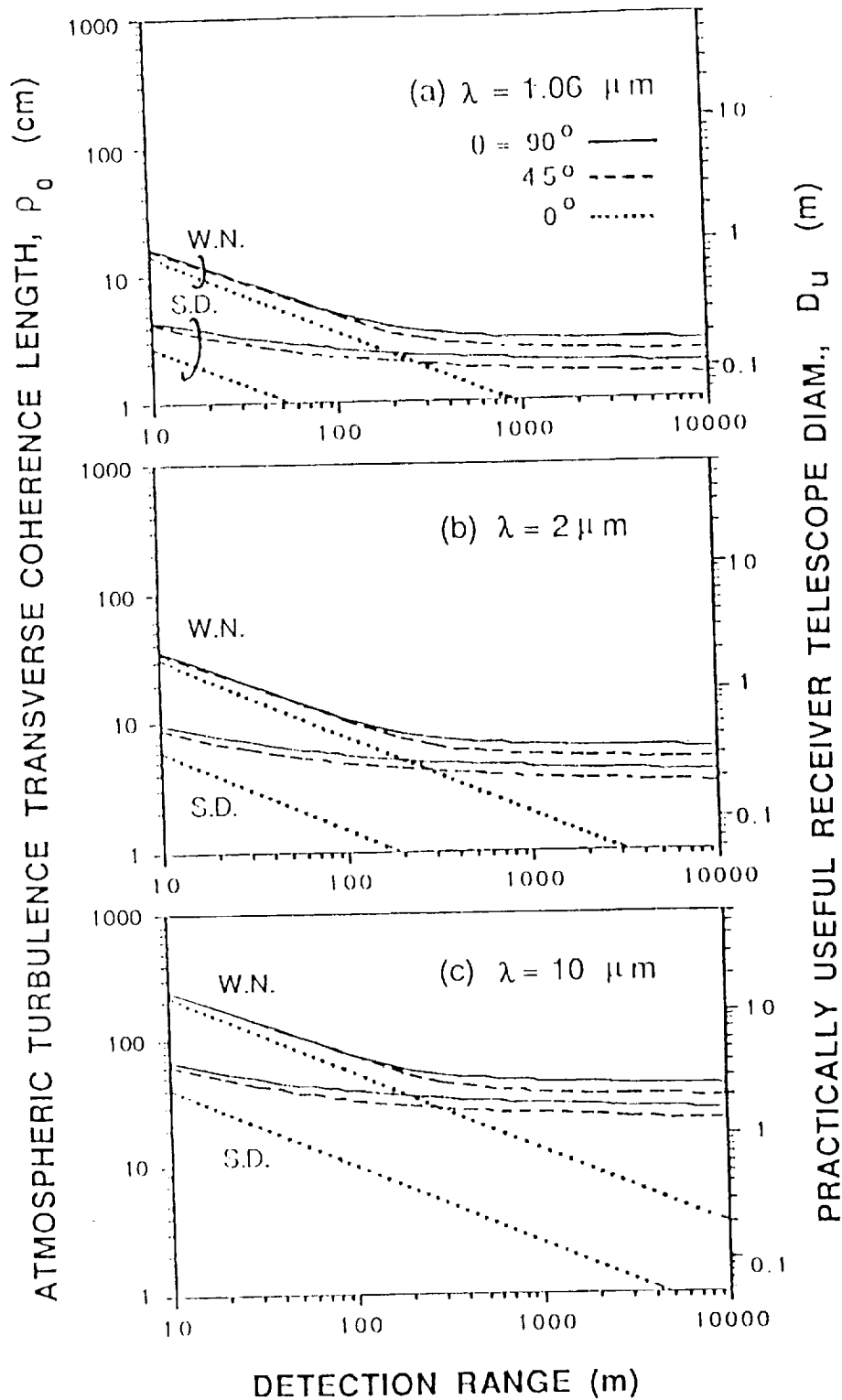


Fig. 5 Predicted maximum useful Lidar telescope size for a Coherent Doppler Lidar as a function of wavelength, slant angle, Lidar range, and turbulence level.

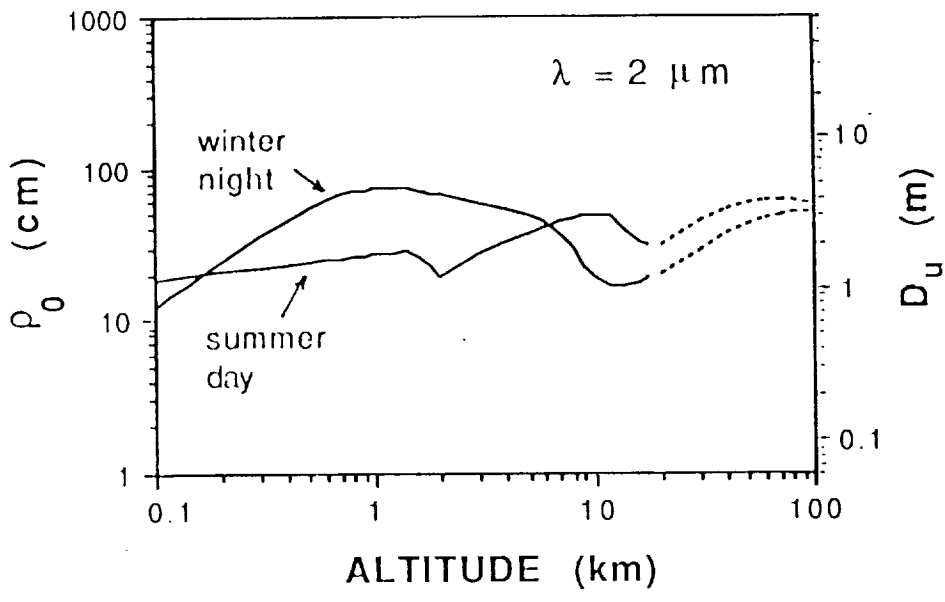


Fig. 6 Predicted maximum Coherent Lidar telescope size for a 2.1 μm Ho Lidar in a satellite orbit and looking downward.

2.3 Diurnal Measurements of C_n^2 for KSC Lidar Measurements

A C_n^2 scintillometer instrument was obtained on loan from NOAA and used to measure the level of atmospheric refractive turbulence. This instrument was used to compare and validate our 1 μm Coherent Lidar measurements and the Ho direct-detection Lidar measurements. Recently, we used this instrument in support of a related 1 μm Coherent Doppler Lidar Wind-Shear measurement test by NASA/LaRC (D. Moerder) and Lockheed (R. Targ and J. Hawley) at KSC during a recent (Sept. 12, 1991) Shuttle Launch. The values of C_n^2 obtained are shown in Fig. 7. As can be seen, the value of the turbulence level varies dramatically during the day. Fig. 8 shows the predicted maximum useful telescope aperture for the upward-looking 1 μm Lockheed Lidar system using the data of Fig. 8. As can be seen, the 20 cm diameter Lockheed Lidar was probably not affected by atmospheric turbulence, due to its upward (verticle) looking Lidar beam direction. Details of these measurements are contained in a Masters Thesis² and are being prepared for publication.

2.4 Joint Development of Single-Frequency Ho Laser/Lidar

A joint program has been initiated with NASA/LaRC (M. Storm, N. Barnes) and USF in the construction/development of a single-frequency Ho laser/Lidar. NASA has developed a preliminary version of the laser and delivered it (on loan) to USF for system testing and laser modifications. The Ho laser consists of a diode-pumped Ho:YAG CW laser and a Q-switched, flashlamp pumped Ho:YAG amplifier. We have recently been in the process of characterizing this laser and modifying the cavity design, in consultation with M. Storm. Our preliminary results indicate that the diode-pumped Ho:YAG laser operates multi-frequency on the 2.09 μm Ho line, but operates single-frequency on the 2.12 μm line; this is done by tuning the temperature of the Ho crystal. We are currently working on

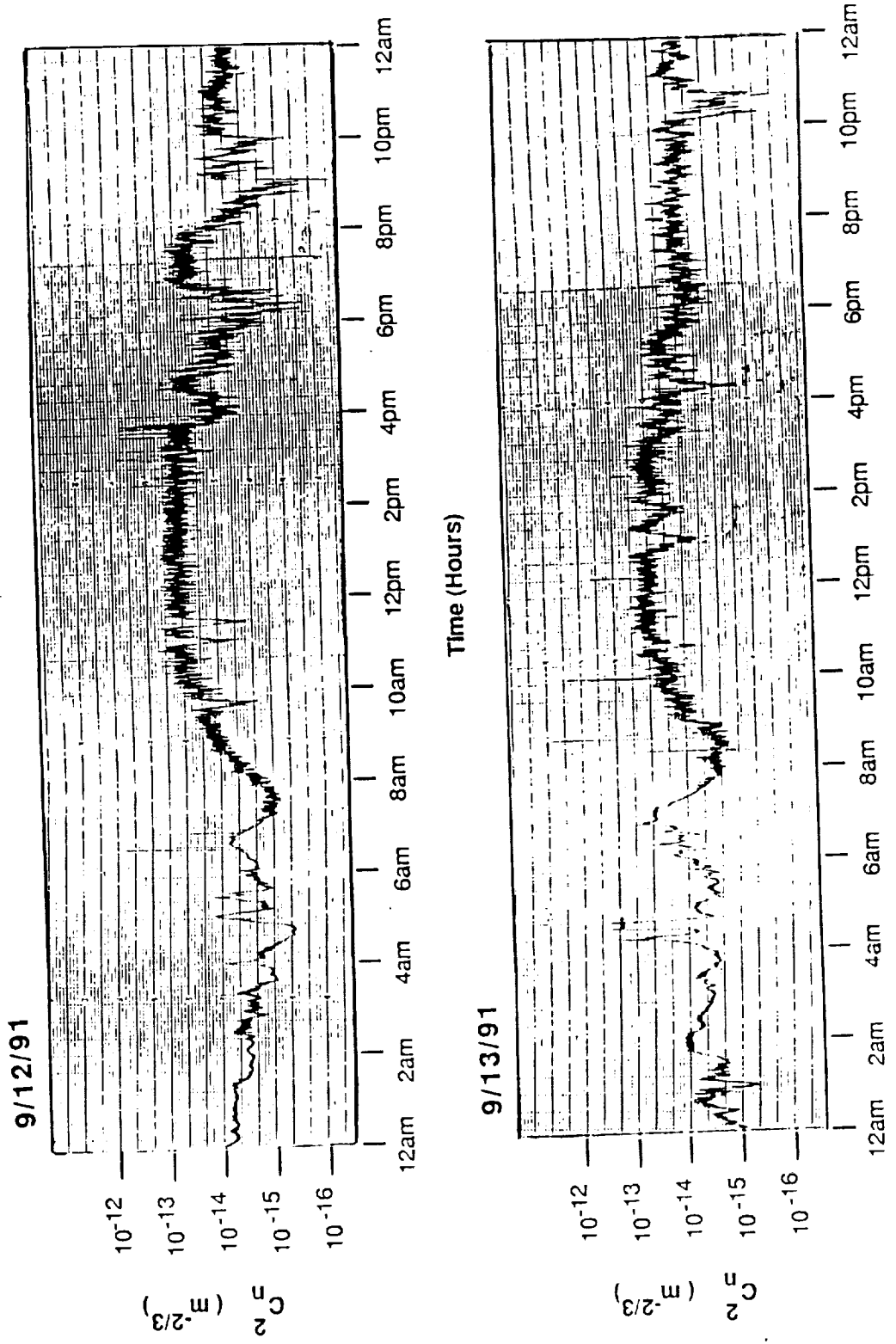


Figure 7. C_n^2 Data Collected at KSC on 9/12/91 and 9/13/91.

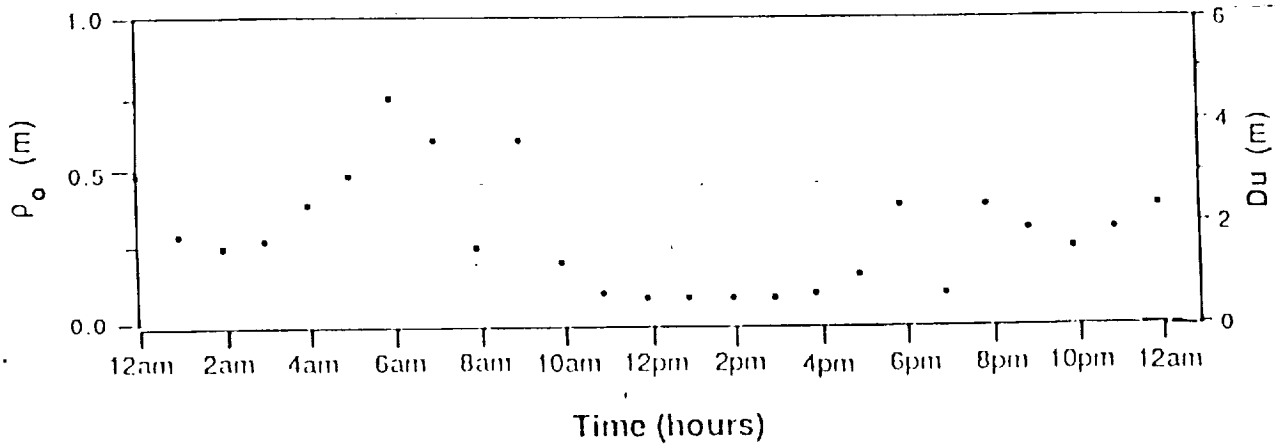


Fig. 8a Predicted Diurnal Variation of Coherence Length, ρ_o , and Effective Telescope Diameter, D_u , for a 1 μm Coherent LIDAR (Data for 9/12/91).

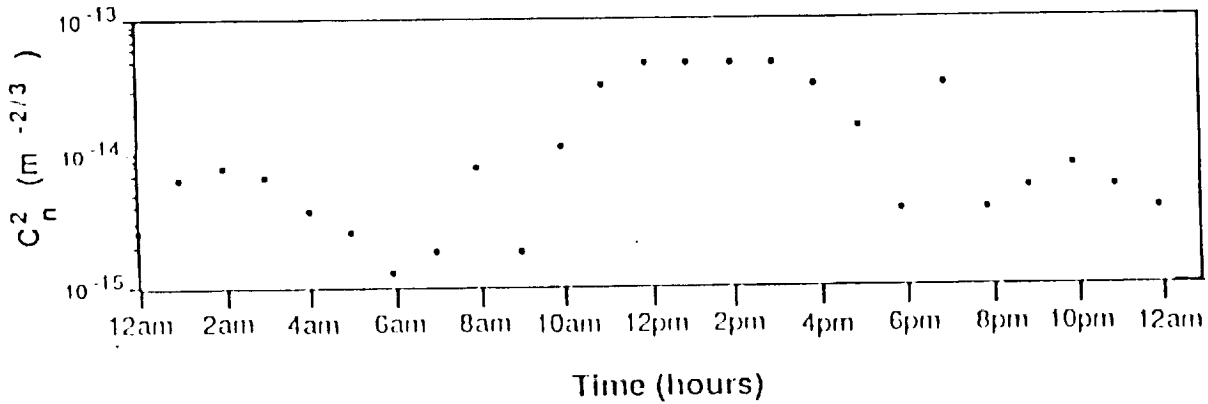


Fig. 8b Measurements Showing the Diurnal Variation of C_n^2 at KSC for 9/12/91.

Ho Laser Output VS Pump Energy
Rep. Rate = 1 Hz
(Q-Switching, TEM00)

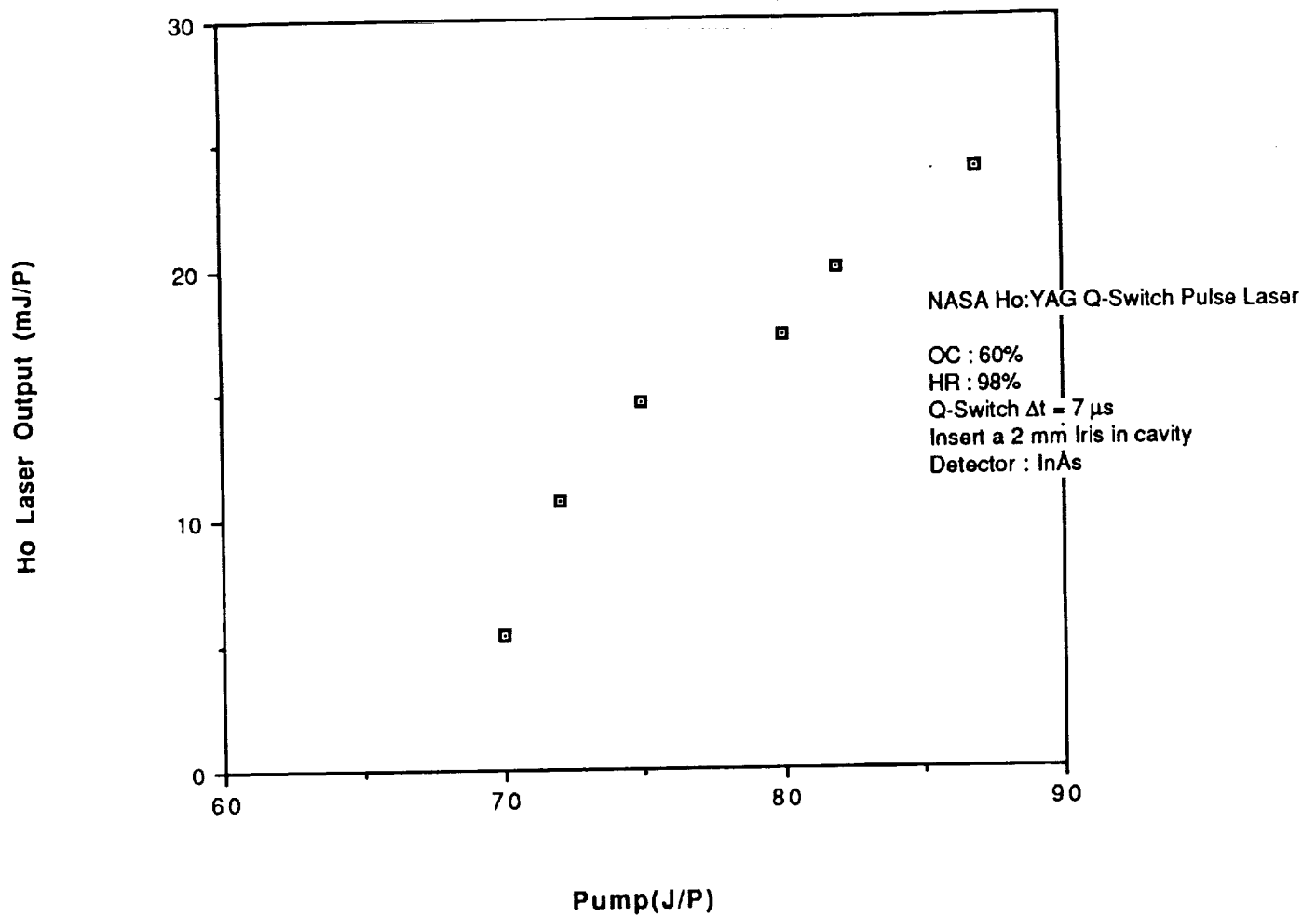


Fig. 9 Output power of modified NASA/LaRC Ho:YAG flashlamp laser

modifying the diode-pumped Ho laser to operate single-frequency on the 2.09 μm line, since this line has higher gain than the 2.12 μm line.

The flashlamp cavity has been considerably modified by using a different optical mounts and cavity assembly. The output of the flashlamp Ho laser is shown in Fig. 9, which indicates that approximately 24 mJ/pulse, TEM₀₀, Q-switched laser pulses were obtained; close to 100 mJ/pulse was obtained for non TEM₀₀ operation. Work is now being conducted in injection seeding the flashlamp Ho:YAG laser using the 2.12 μm line; operation at 2.09 μm will also be studied. Future plans include using this laser in our Ho Lidar system and the operation of the system for Coherent Lidar measurements of the atmosphere. It is anticipated that Lidar measurements of atmospheric winds will be made in order to quantify the potential sensitivity of the Ho Doppler Lidar for wind detection.

3. ANTICIPATED FUTURE PROGRAM TASKS

Future program tasks for FY91-FY92 will include (1) continued development of single-frequency Ho:YAG laser source in conjunction with NASA/LaRC, (2) incorporation of Ho:YAG laser into a Coherent Doppler Lidar system, (3) investigation of use of 2-D heterodyne detector arrays to improve Ho Coherent Lidar performance, and (4) joint development/incorporation of Ho:YLF laser source into Ho Lidar system. This latter task is related to the current NASA/LaRC development of a high-power, diode-pumped Ho:YLF laser source for atmospheric Lidar.

It is anticipated that the Ho:YLF laser may have to be slightly tuned in wavelength in order to increase its transmission through the atmosphere. This can be seen in Fig. 10, which is a plot of the transmission of the atmosphere over a 10 km path (ground level) and the overlap of the tuning range of the lines for Ho:YAG, Ho:YSGG, and Ho:YLF. Further studies will be made in order to verify the above predictions with actual DIAL/Lidar atmospheric measurements.

ORIGINAL PAGE IS
OF POOR QUALITY

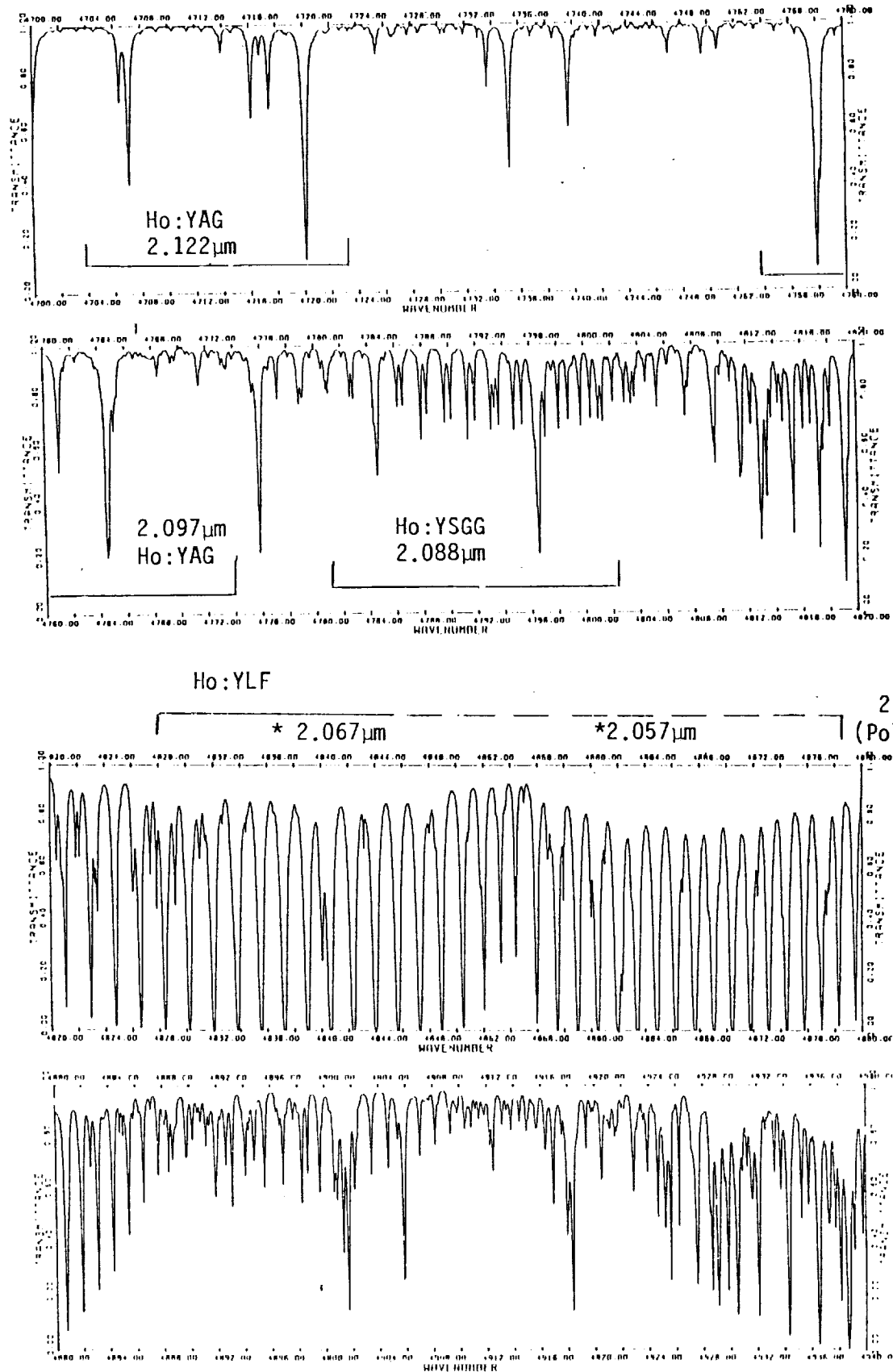


Fig. 10 Atmospheric transmission through 10 km path (sea level) showing overlap of tuning range of Ho:YAG, Ho:YSGG, and Ho:YLF laser lines.

4. REFERENCES

1. Enhanced detection of atmospheric turbulence distorted 1 μm coherent lidar returns using a two-dimensional heterodyne detector array, K.P. Chan and D.K. Killinger, Optics Letters 16, 1219 (1991).

2. Diurnal Measurements of Atmospheric Optical Turbulence with applications to Coherent Lidar, William E. Wilcox, Jr., Master Thesis (Physics Dept., University of South Florida) Nov., 1991.

5. APPENDICES

The following papers are reprints of journal articles published in part with support from the NASA/LaRC program. They document details of the progress reported in the above sections.

Appendix 1 (Reprint of article in Japanese Journal of Optics, 20,612 (1991))

**Performance Characteristics of Acousto-Optic Q-switched
Tunable 2.1 μm Ho: YSGG Laser**

Yasunori SAITO, Kin Pui CHAN and Dennis K. KILLINGER



Performance Characteristics of Acousto-Optic Q-switched Tunable 2.1 μm Ho: YSGG Laser

Yasunori SAITO, Kim Pui CHAN and Dennis K. KILBINGER

Department of Physics, University of South Florida,
Tampa, Florida 33620, U.S.A.

(Received March 27, 1991; Accepted June 29, 1991)

This technical note documents the performance characteristics of a flashlamp pumped, acousto-optic (A/O) Q-switched, 2.1 μm Cr: Tm: Ho: YSGG laser. A fused quartz A/O Q-switch was inserted in the Ho laser cavity between the laser rod and the rear mirror, and was modulated by a RF signal of 27.1 MHz. The Q-switched laser pulse energy and pulse width were measured as a function of the delay time of the A/O Q-switch signal, flashlamp input energy, and Ho laser rod temperature. At optimal operating conditions, the Ho: YSGG laser pulse had a pulse energy of 25 mJ and a pulse width of 88 ns; this was obtained with a flashlamp input energy of 156 J, temperature of 16°C, and repetition rate of 3 Hz. Continuous tuning of the Ho laser was obtained over a range from 2.081 μm to 2.087 μm using two uncoated glass intracavity etalon. The linewidth of the laser was approximately 0.1 nm.

1. Introduction

IR tunable solid-state lasers doped with rare earth and transition metals like Er, Ho, Tm, Cr, and Ti are currently being developed, because these lasers have the potential for diode laser pumping, wide tunability, and high average power.¹⁾ We are interested in the development of the 2.1 μm Ho laser as a light source for laser remote sensing of the atmosphere. The Ho laser operates in the so called "eye-safe" spectral region ($\lambda = 1.4 \mu\text{m}$) and is also tunable over a 0.01 μm range near 2.1 μm . This wavelength coincides with several water vapor absorption lines in the atmosphere. Because of these potential attributes, the Ho laser is being actively developed for DIAL (differential-absorption lidar) measurements of water vapor in the atmosphere^{2,3)} and for coherent Doppler lidar measurements of atmospheric winds for LAWS (NASA/LIDAR Atmospheric Wind Sounder).⁴⁾

For long-range, range-resolved lidar and DIAL applications, a laser pulse of high peak power and short duration is required, which can be obtained only through Q-switched operation of the laser. In the case of the Ho laser, Q-switching techniques have included a mechanical spinning mirror and also a LiNbO₃ po克尔 cell.⁵⁻⁷⁾ These

techniques have some limitations in the operation of the Ho laser. The spinning mirror Q-switch has mechanical vibrations and the repetition rate of the laser is limited by the rotation frequency of a motor. The LiNbO₃ Q-switch has problems due to optical damage at high fluence levels if the Q-switch has any residual absorption in the IR wavelength region. Another technique for Q-switching a pulsed laser is to use an acousto-optic (A/O) Q-switch; this technique only works if the gain of the laser cavity is small to moderate, since A/O Q-switches do not normally have exceptional "hold-off" capability. In spite of this limitation, an A/O Q-switch has been used successfully in a lower-power diode laser pumped Ho: YAG laser⁸⁾ and has also just recently been used in a higher power flashlamp pumped Ho laser.

In this short technical note, we describe our experimental testing of a commercial Ho laser which used an A/O Q-switch and document for the first time its performance parameters. Our results indicate that the optimal Ho laser performance was obtained at a Ho laser rod temperature of 16°C, a Q-switch delay time of 630 μs , and at an input flashlamp pump energy of approximately 160 J/pulse. Output energy of the Ho laser pulse was approximately 25 mJ and the laser pulse width was 88 ns.

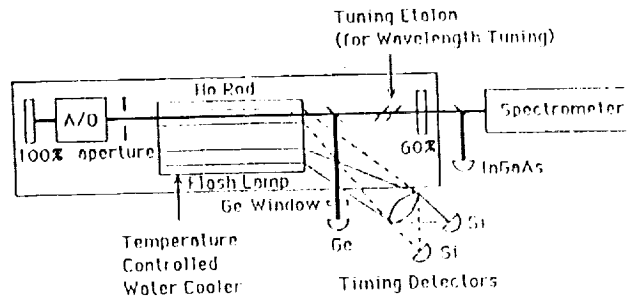


Fig. 1 Schematic diagram of the Ho laser.

2. Experimental Setup

The laser used in this experiment was a commercially available, flashlamp pumped, Ho: YSGG laser (Schwartz Electro-Optics, Laser 1-2-3); a schematic diagram of the laser is shown in Fig. 1. The laser cavity used a 5 mm \times 75 mm Ho: YSGG rod with Cr and Tm co-doping to aid in flashlamp operation; the concentration was $5 \times 10^{21} \text{ cm}^{-3}$ Ho, $2 \times 10^{21} \text{ cm}^{-3}$ Cr, and $8 \times 10^{20} \text{ cm}^{-3}$ Tm. The laser cavity had a 100% reflection rear mirror, 60% reflection output mirror, and a cavity length of 67 cm. A fused quartz A/O Q-switch (Newport Electro-Optics Systems, Model No. N 32027-50-5-2-1) was used in the laser cavity and was modulated with a radio frequency (RF) signal of 27.1 MHz supplied by an RF driver (Newport Electro-Optics Systems, Model No. N 31027-50 DM). The A/O device was placed between the rear mirror and the laser rod. An aperture was inserted between the A/O device and the rod to achieve TEM₀₀ single spatial mode laser operation. The pulse energy was measured with an energy meter and the shape of the Q-switch pulse was monitored using a fast rise-time InGaAs (Epitaxx, Model No. ETX 1000 GR 21) photodetector with a high speed amplifier (Analog Module, Model No. 313-1 S). The wavelength of the laser was monitored by a 0.5 m grating spectrometer.

The relative timing of the flashlamp, the build-up of the population inversion of the Ho atoms, and the Q-switch trigger pulse are important in determining the output characteristics of the Ho laser. In order to measure some of these temporal parameters, a Ge detector (with a Ge window) was used in the cavity in order to measure the 1.8 μm fluorescence from the Ho laser rod, a Si detector was used adjacent to the flashlamp to measure the visible output of the flashlamp, and another Si detector was used to measure the green fluorescence from the laser rod. An InGaAs detector monitored

the laser output pulse.

3. Results

Figure 2(a) shows a composite photograph of the relative timing of the detected optical and elec-

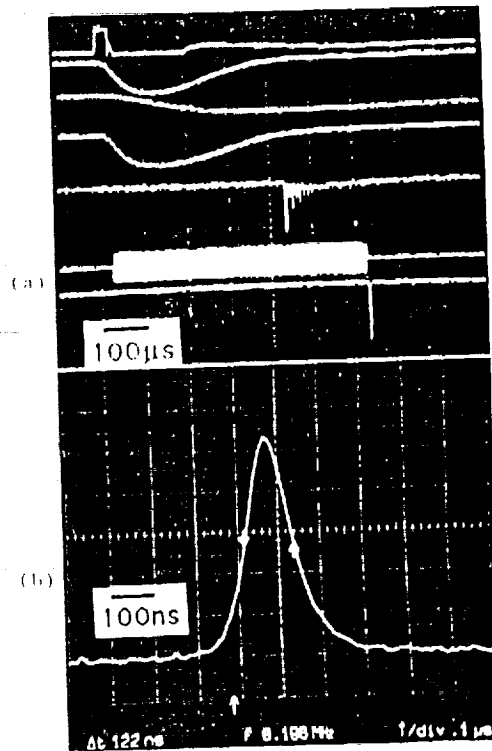


Fig. 2 (a) Photograph of the relative timing of the flashlamp trigger, flashlamp visible output, Ho fluorescence near 1.8 μm , Ho fluorescence in the green wavelength range, normal mode oscillation of the Ho laser (without A/O Q-switch), RF drive signal to the A/O Q-switch, and the Q-switched laser pulse. (b) Photograph of the pulse shape of the Q-switched Ho laser. Laser conditions are flashlamp input energy of 121 J, Ho laser rod temperature of 16 $^{\circ}\text{C}$, and repetition rate of 3 Hz.

trical signals. The signals show, in order from top to bottom, the relative timing of the flashlamp trigger, flashlamp visible output, Ho fluorescence near $1.8 \mu\text{m}$, Ho fluorescence in the green wavelength range, normal mode oscillation of the Ho laser (without Q-switch), the RF drive signal to the Λ/O Q-switch, and the Q-switched Ho laser pulse. It should be noted that the signal obtained from the $1.8 \mu\text{m}$ Ho fluorescence is indicative of the measured 3.5 ns lifetime of this level and is similar to that reported previously.^{5,7} The strong green fluorescence is due to the $^5\text{S}_2\text{-}^5\text{P}_2$ transition in Ho.⁷ Figure 2(b) shows a more detailed pulse shape of the Q-switched Ho laser pulse.

The pulse energy and pulse width of the Q-switched laser pulse were found to be strongly dependent upon the delay time of the Λ/O Q-switch RF turn-off time. This is shown in Fig. 3 which shows the measured pulse energy as a function of the delay time. The optimal delay time was found to be approximately 630 μs for our experimental setup. Our laser had the following operational parameters: TEM₀₀ mode, 12 mJ laser pulse energy, 120 ns pulse length, flashlamp input energy of 121 J/pulse, and Ho rod temperature of 16°C. An aperture of 3 mm was used to force the laser output into a TEM₀₀ mode. The pulse energy for Q-switched multimode operation was 29 mJ/pulse and for normal oscillation (no Q-switch) was 37 mJ/pulse. Laser threshold was 96 J for the flashlamp energy. As seen in Fig. 3, the laser output is maximum at a pulse repetition frequency (PRF) of 3 Hz with a decrease seen at 4 Hz; a significant decrease was also observed at 5 Hz due to an increase in the thermal lens effect at the higher PRF values.

The Q-switched pulse width was also measured

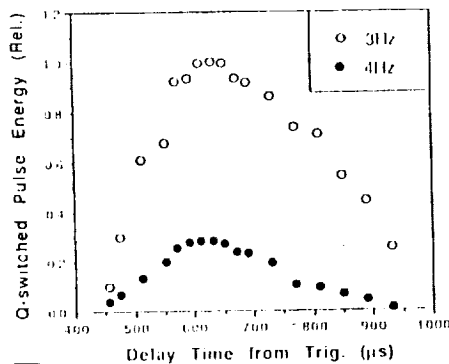


Fig. 3 Q-switched pulse energy as a function of the Q-switch delay time from the flashlamp trigger.

as a function of the Q-switch delay time and is shown in Fig. 4. As can be seen, the shortest pulse length occurs at the delay time for the highest output power which is as expected. It should be added that because the transfer of excitation in the laser rod involves the Cr and Tm ions also, the Ho population inversion can also occur at significant delay time.⁸ This long term excitation process can produce a secondary (or double) pulse which occurs much later in time after the Q-switched pulse. In order to eliminate this double pulse, the RF drive to the Q-switch was turned "back-on" after approximately 1.5 μs at the end of the regular RF drive pulse. This is not shown in Fig. 2 for ease of clarity in explaining the relative timing of the Ho laser.

The output energy and pulse width of the Ho laser were also investigated as a function of the flashlamp input power and operating temperature of the Ho laser rod. Figure 5 shows the measured

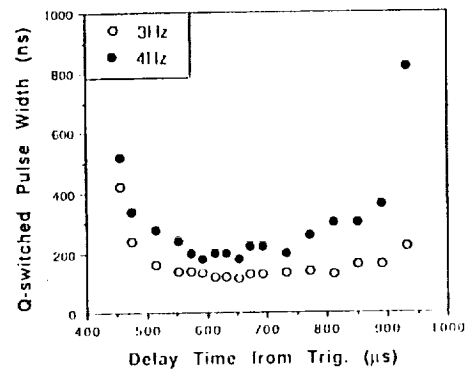


Fig. 4 Q-switched pulse width as a function of the delay time from the flashlamp trigger.

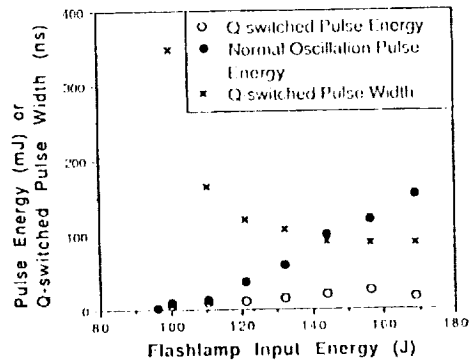


Fig. 5 Pulse energy (mJ) for the both normal oscillation and Q-switched operation, and the Q-switched pulse width (ns) as a function of flashlamp input energy.

laser output pulse energy for both normal oscillation and Q-switched operation, and the measured Q-switched pulse width. As seen in Fig. 5, at the higher flashlamp input levels, the TEM₀₀ mode Q-switched laser pulse had a pulse energy of 25 mJ and a pulse width of 88 ns with a flashlamp input energy of 156 J. The normal oscillation pulse energy increased to nearly 150 mJ/pulse at the higher input levels but the Q-switched output power did not significantly increase. While this may be indicative of the relatively low saturation fluence of the Ho laser, it may be also due to losses in our A/O Q-switch. We are currently studying this more in order to improve the Q-switched output power.

Figure 6 shows the Q-switched pulse energy and pulse width as a function of the laser rod temperature. As can be seen, an operational temperature near 16°C seems to optimize the output power of the Ho laser with a concurrent reduction in the laser pulse width. It may be added that, in general, the threshold energy of the Ho laser is decreased when the rod is cooled because the population of the lower state laser level of Ho is lowered.³⁾ The optimal temperature is dependent upon several experimental conditions, including the rod geometry, cooling design, related thermal aspects, heat load of the flashlamp, and laser energy extraction efficiency. In our experiments, the optimal temperature was found to be near 16°C, although this value will change slightly for different PRF and flashlamp input energy.

We have also studied the tunability of the Ho laser. Two uncoated glass etalons (0.2 mm and 1.0 mm thickness) were inserted in the Ho laser cavity between the output mirror and the laser rod. The

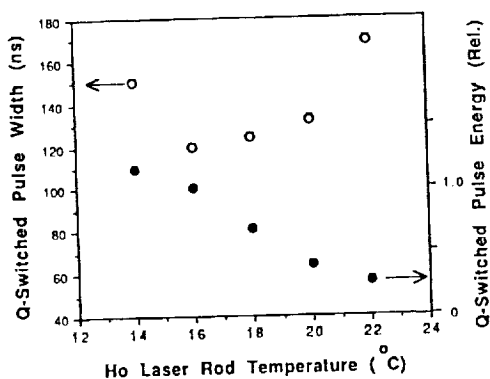


Fig. 6 Q-switched pulse energy and Q-switched pulse width as a function of the laser rod temperature.

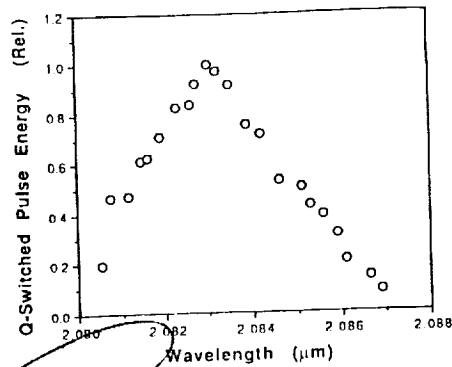


Fig. 7 Tuning curve of the Ho laser.

measured tuning curve is shown in Fig. 7 which indicates that the Ho laser can be tuned smoothly from 2.081 μm to 2.087 μm ; the linewidth of the laser was measured to be approximately 0.1 nm. These tuning results are similar to our previously reported results.³⁾ It is informative to mention that the wavelength of the Ho: YSGG laser is similar, but not exactly the same, to that of the Ho: YAG laser. Recently, Henderson and Hale¹⁶⁾ have shown that the Ho: YAG laser operates on two closely spaced lines at 2.090 μm and at 2.097 μm , with tuning obtained from 2.088 to 2.098 μm .

4. Conclusion

In this technical note, we have documented our studies of the operational characteristics of a flashlamp pumped A/O Q-switched Cr: Tm: Ho: YSGG laser operating on the 2.1 μm Ho laser line. Typical operating parameters of the Q-switched laser were pulse energy of 25 mJ and a pulse width of 88 ns with a flashlamp input energy of 156 J, temperature of 16°C, and repetition rate of 3 Hz. The pulse energy was somewhat greater than that obtained previously using a spinning mirror Q-switch.³⁾ Continuous tuning of the Ho laser was also obtained over a range from 2.081 μm to 2.087 μm .

Our future plan is to injection seed our Ho laser in order to have it operate as a tunable single-frequency laser source. Such operation will permit it to be used in a Doppler lidar system as well as a differential-absorption lidar for atmospheric water vapor and CO₂ measurements.

Acknowledgement

This work was supported in part by NASA/Langley Research Center and by the Florida High Technology and Industry Council. Yasunori Saito is a visiting scientist from Shinshu University, Nagano, Japan.

References

- 1) *Advanced Solid-State Lasers*, Technical Digest, OSA Topical Meeting, Salt Lake City (1990).
- 2) N. Sugimoto, N. Sims, K. P. Chan and D. K. Killinger: "Eye-safe 2.1 μ m Ho lidar for measuring atmospheric density profiles," *Opt. Lett.*, **15** (1990) 302-304.
- 3) S. Cha, K. P. Chan and D. K. Killinger: "Tunable 2.1 μ m Ho lidar for simultaneous range-resolved measurement of atmospheric water vapor and aerosol backscatter profiles," *Appl. Opt.* (1991) in press.
- 4) S. W. Henderson, C. P. Hale, J. R. Magee, M. J. Kavaya and A. V. Huffaker: "Eyesafe coherent laser radar system at 2.1 μ m using Tm, Ho: YAG lasers," *Opt. Lett.*, **16** (1991) 773-775.
- 5) N. P. Barnes and D. J. Gettemy: "Pulsed Ho: YAG oscillator and amplifier," *IEEE J. Quantum Electron.*, **QE-17** (1981) 1303-1308.
- 6) T. J. Kane and T. S. Kubo: "Diode-pumped single-frequency lasers and Q-switched lasers using Tm: Ho: YAG," *Advanced Solid-State Lasers*, OSA Topical Meeting (Ref. 1) (1990) pp. 133-135.
- 7) T. Y. Fan, G. Huber, R. L. Byer and P. Mitzscherlich: "Spectroscopy and diode laser-pumped operation of Tm, Ho: YAG," *IEEE J. Quantum Electron.*, **QE-24** (1988) 924-933.
- 8) G. J. Quarles, A. Rosenbaum and C. L. Marquardt: "High-efficiency 2.09 μ m flashlamp-pumped laser," *Appl. Phys. Lett.*, **55** (1989) 1062-1064.
- 9) R. L. Remski and D. J. Smith: "Temperature dependence of pulsed laser threshold in YAG: Er³⁺, Tm³⁺, Ho³⁺," *IEEE J. Quantum Electron.*, **QE-6** (1970) 435-440.
- 10) S. W. Henderson and C. P. Hale: "Tunable: single-longitudinal mode diode laser pumped Tm: Ho: YAG laser," *Appl. Opt.*, **29** (1990) 1716-1718.

Tunable 2.1- μm Ho lidar for simultaneous range-resolved measurements of atmospheric water vapor and aerosol backscatter profiles

Sungdo Cha, Kin Pui Chan, and Dennis K. Killinger

An eye-safe, tunable differential-absorption lidar system has been developed for the range-resolved measurement of aerosol backscatter and water vapor in the atmosphere. The lidar uses a flash-lamp-pumped, Q-switched, 10-mJ solid-state Ho:YSGG laser that is continuously tunable over a 20-cm⁻¹ wavelength range near 2.084 μm . Both path-averaged and range-resolved measurements were performed with the Ho differential-absorption lidar system. Preliminary measurements have been made of the temporal variation of atmospheric aerosol backscatter and water-vapor profiles at ranges out to 1 km. These results indicate that the Ho lidar has the potential for the eye-safe remote sensing of atmospheric water vapor and backscatter profiles at longer ranges if suitably enhanced in laser power and laser linewidth.

I. Introduction

Recently there has been increased interest in the development of an eye-safe, solid-state laser-lidar system for the detection of wind shears in front of aircraft and for the remote sensing of water vapor in the atmosphere.¹⁻³ The 2.1- μm Ho laser is considered to be potentially well suited for these lidar applications because it is eye safe ($\lambda > 1.4 \mu\text{m}$), can be pumped by diode lasers, and offers the potential for tunability.⁴

Previously we reported the development of a Ho lidar and the range-resolved remote sensing of atmospheric aerosol backscatter profiles at ranges out to 2 km.⁵ In this paper we report an extension of this work that includes the precision tuning of our low-power (10 mJ/pulse) Ho laser over a 20-cm⁻¹ wavelength range. The continuous-tuning coverage was measured from 2.080 to 2.089 μm ($\sim 90 \text{ \AA}$) and also from 2.104 to 2.106 μm . The wavelength range of 2.080–2.089 μm overlaps several absorption lines of water vapor so that the Ho laser can be used for the differential-absorption lidar (DIAL) remote sensing of water vapor in the atmosphere. As an initial demonstration of the potential utility of the Ho lidar-DIAL system, the atmospheric

aerosol backscatter and water-vapor concentration profiles were measured simultaneously at ranges out to 1 km as a function of time during the day. This is to our knowledge the first DIAL measurement of atmospheric water vapor made with the Ho laser and shows that the Ho DIAL system may be potentially well suited for the detection of both aerosol backscatter and water-vapor concentration profiles in the atmosphere. Our experimental results indicate that future extension of the Ho laser to higher power, of the order of 1 J/pulse, should provide up to tens of kilometers detection range.

It should be added that our range-resolved lidar measurements of atmospheric water vapor and aerosol backscatter represent an extension of previous work by us and by others. Previously Baker,⁶ Hardesty,⁷ and Grant *et al.*⁸ measured water-vapor profiles by using CO₂ lasers, while Browell *et al.*⁹ and Ehret *et al.*¹⁰ used dye lasers tuned in the near-IR spectral region. Of course, early research by Schotland¹¹ and by Zuev *et al.*¹² showed the first use of a solid-state (ruby) laser source for DIAL measurements of water vapor, as did our recent research that used a Co:MgF₂ solid-state laser.¹³ What is novel about our Ho DIAL research presented in this paper is that the Ho laser is believed to offer several advantages over these previous laser sources, namely, that it can be pumped by diode lasers, it operates in the eye-safe wavelength range, and the atmospheric backscatter coefficient at 2.1 μm is greater than that at 10 μm . Thus the Ho lidar has the potential to be important not only for atmospheric aerosols and water-vapor profiling but also for three-dimensional Doppler mapping of wind velocity.

The authors are with the Department of Physics, University of South Florida, Tampa, Florida 33620.

Received 20 August 1990.

0003-6935/91/273938-06\$05.00/0.

© 1991 Optical Society of America.

II. Ho:YSGG DIAL System

In this section we describe wavelength tuning of the Ho laser by an intracavity étalon and the Ho DIAL system. The Ho DIAL system consisted of a tunable Ho:YSGG laser, spectrometers to monitor the laser wavelength, lidar optics (a beam-steering mirror and a receiving telescope), optical detectors, and a data-acquisition system to record the lidar return signals. A schematic of the Ho DIAL system is shown in Fig. 1. This Ho lidar is essentially the same as reported previously⁵ with the addition of the laser-tuning elements and associated wavelength monitors.

A. Wavelength Tuning of the Ho Laser

Previous research on the 2.1- μm Ho laser has shown that the Ho laser can be used for tunable DIAL applications. First the Ho laser has been shown by Johnson *et al.* to operate on several different emission lines over a wavelength range of $\sim 2.09\text{--}2.12\ \mu\text{m}$.¹⁴ Barnes and Gettemy showed that a grating could be used to tune the Ho:YAG laser over each of these emission lines with a tuning range of $\sim 30\ \text{cm}^{-1}$ (i.e., $0.013\ \mu\text{m}$).¹⁵ More recently Henderson and Hale have shown diode laser-pumped, single-frequency operation of a cw Tm:Ho:YAG oscillator, which indicated the potential of the oscillator as a narrow spectral laser source.¹⁶ Our development of the tunable Ho laser used a commercial flash-lamp-pumped Ho laser (Schwartz Electro-Optics, Model Laser 1-2-3) with a Ho:YSGG laser rod; Ho:YSGG was used instead of Ho:YAG because of its immediate availability.

When the laser was operated in a non- Q -switched mode, its output pulse length was $250\ \mu\text{s}$ with 20-mJ pulse energy. In the Q -switch operation using a spinning mirror, the pulse length was 200 ns with $\sim 10\text{-mJ}$ pulse energy. The pulse repetition rate was limited primarily by the spinning mirror Q switch and was 2 Hz. The wavelength of the laser output was monitored by a 0.5-m spectrometer and a 2.1- μm sensitive TV video camera, which is described in more detail below.

In the initial experimental setup, the tuning of the Ho laser was accomplished by using a single, uncoated glass étalon in the laser cavity. The laser wavelength was changed by varying the tilt angle of the étalon. The measured tunable wavelength range of the Ho:YSGG laser using the intracavity étalon (thickness 0.17 mm) is shown in Fig. 2(a). The wavelength of the Ho laser was tuned continuously from 2.080 to 2.089 μm in single-transverse-mode (TEM_{00}) operation and was also tuned near the 2.105- μm line in multimode operation. The latter line has a lower gain than the 2.08- μm line but shows greater output power in Fig. 2(a) because multimode operation uses a much larger active mode volume in the laser rod than does the TEM_{00} mode. The tuning range of the multimode Ho laser was measured from 2.1040 to 2.1064 μm . This tunable spectral range is consistent with previous fluorescence emission data for Ho.¹⁷ It should be noted that single, uncoated glass étalons with thicknesses of 0.1 and 0.2 mm, respectively, were also tried; the wave-

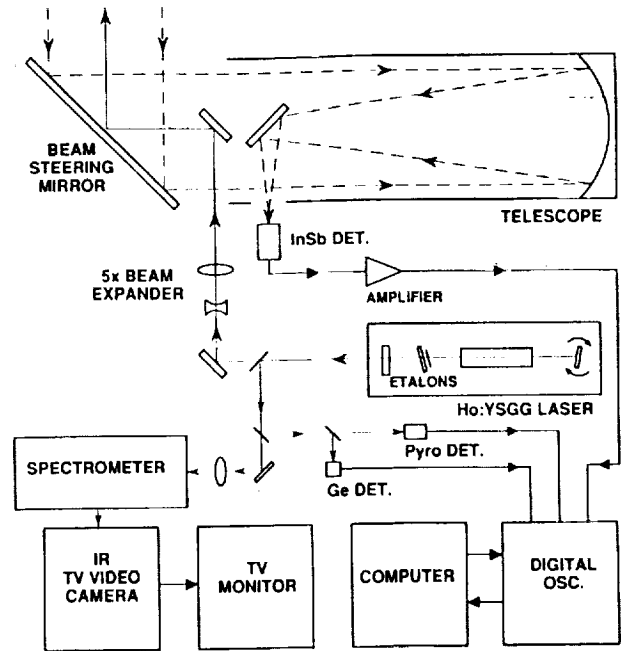


Fig. 1. Schematic of the Ho lidar-DIAL system; Det, detector; pyro, pyroelectric.

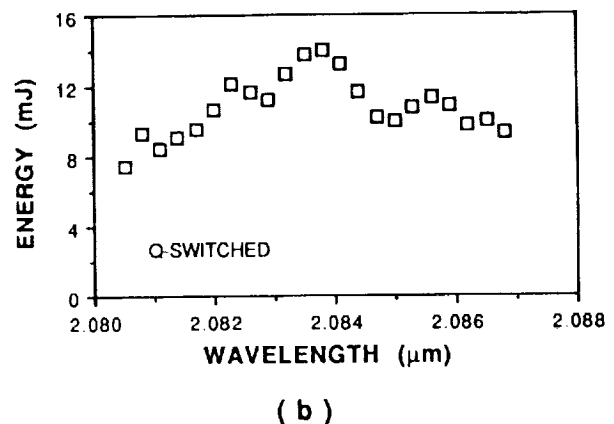
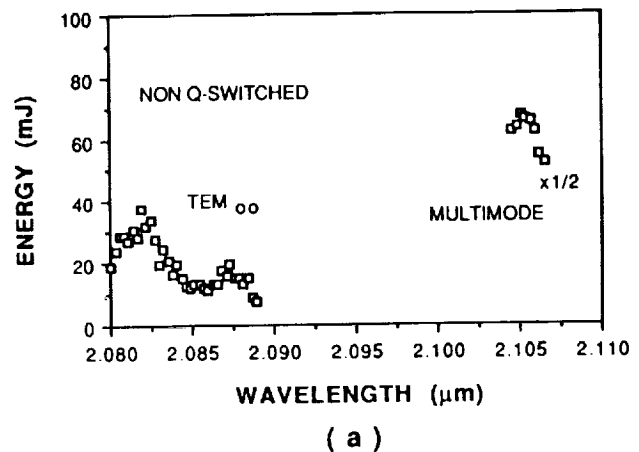


Fig. 2. Measured tuning range of the Ho:YSGG laser using tilted intracavity étalons. (a) One étalon (thickness 0.17 mm) was used in the non- Q -switched laser cavity. (b) Two étalons (thicknesses 0.2 and 1.0 mm) were used in the Q -switched laser cavity.

length tuning range was measured to be ~ 80 and 70 \AA . By using the 0.17-mm étalon, the linewidth of the laser was reduced from 3 to 0.46 cm^{-1} .

In our initial experiments it was noticed that the tuning of the Ho-laser wavelength was not completely smooth but occurred in a series of étalon mode hops with a spacing between wavelengths of $\sim 3 \text{ \AA}$ (0.68 cm^{-1}). It was determined that the output coupler of the Ho laser was acting as an étalon. The output coupler was made of ZnSe (thickness 3 mm , reflectivity 70%) with flat, plane-parallel surfaces and had a calculated free-spectral range as an étalon of $\sim 3 \text{ \AA}$. Several different thicknesses and types of output coupler were also tried, which confirmed this hypothesis. As a result, a 1° wedged output coupler was used and produced a smooth tuning of the laser wavelength within the accuracy of our spectral-measurement resolution.

To reduce the linewidth of the Q-switched Ho laser even further, two uncoated glass étalons (thicknesses 0.2 mm and 1.0 mm) were mounted on a single rotating stage and placed in the Ho-laser cavity. To eliminate mode hopping over the transmission modes of the thicker étalon, the transmission peaks of the two étalons were adjusted to the same position in the wavelength domain. This was done by careful adjustment of the tilt angles of the two étalons relative to each other while the laser output wavelength was monitored. By this method the étalon spectral modes were aligned to provide for smooth tunability and relatively narrow linewidth. The resultant tunable wavelength range of the TEM₀₀, Q-switched Ho laser is shown in Fig. 2(b). As can be seen, the tuning was smooth and ranged from ~ 2.080 to $2.087 \text{ }\mu\text{m}$. The laser linewidth (FWHM) was found to be $\sim 0.23 \text{ cm}^{-1}$ as measured by a precision scanning Fabry-Perot interferometer.

B. DIAL System

Small portions of the laser beam were sampled by a pyroelectric detector and a Ge detector for the monitoring of the laser power and the triggering of the data-acquisition system, respectively. The wavelength of the Ho laser was monitored with a 0.5-m spectrometer used as a spectrograph with the output imaged on a $2.1\text{-}\mu\text{m}$ sensitive TV video camera (Electrophysics Model 7290-06). This arrangement permitted visual observation in real time of the laser wavelength over a range of $\sim 60 \text{ cm}^{-1}$.

The output of the laser was collimated to a beam diameter of $\sim 15 \text{ mm}$ by a $5\times$ beam expander. The main portion of the laser beam was directed with mirrors and aligned in a coaxial configuration with the lidar telescope. The direction of the laser beam was steered by a $40\text{-cm} \times 40\text{-cm}$ mirror. The laser beam was transmitted from our lidar laboratory stationed on the third floor of the laboratory building and aimed horizontally either into the air or toward a building $\sim 1.1 \text{ km}$ away.

The lidar return signals were collected by a 30-cm -diameter Newtonian telescope with a focal length of 1.75 m and a field of view of $\sim 1.2 \text{ mrad}$. The optical detector was a 1-mm -diameter, liquid-nitrogen-cooled

InSb photovoltaic detector (Infrared Associates Model IS-1), which had a cold filter with a $0.35\text{-}\mu\text{m}$ spectral bandwidth. The D^* of the InSb detector was $3.8 \times 10^{11} \text{ cm Hz}^{1/2}/\text{W}$ at $2.1 \text{ }\mu\text{m}$ for a $385\text{-k}\Omega$ load impedance (0.3-MHz bandwidth). For our lidar experiments, the detector electrical output was shunted into a $1.3\text{-k}\Omega$ load impedance that raised the detector-amplifier bandwidth to 5 MHz but lowered the D^* of the InSb detector to $2 \times 10^{10} \text{ cm Hz}^{1/2}/\text{W}$. The output signal from the InSb detector was processed through a 100-MHz preamplifier (Analog Module Model 352-1-S-1M) and recorded by a 100-MHz digital oscilloscope (LeCroy Model 9400) controlled by a Macintosh II computer for signal analysis.

It may be added that, although we used the liquid-nitrogen-cooled InSb detector in all the reported lidar experiments in this paper, we also were able to use a room-temperature (red-extended) InGaAs photodetector (Epitaxx Model EPX1000GR21) combined with a 300-MHz preamplifier (Analog Module Model 313-1-S). It was found that the lidar signal-to-noise ratio (S/N) from the room-temperature InGaAs was only approximately a factor of 4 less than that from the liquid-nitrogen-cooled InSb detector. We believe that thermoelectrically cooling the InGaAs detector and reducing the amplifier bandwidth may result in superior performance by the InGaAs detector over the InSb detection; we are currently studying this.

III. Lidar/DIAL Measurements

Using the lidar system shown in Fig. 1, we measured range-resolved lidar returns from atmospheric aerosol backscatter. In addition, we also measured lidar returns from hard targets to perform path-averaged DIAL measurements of atmospheric water vapor. The single-pulse S/N of the aerosol backscattered return signal was $\sim 6\text{--}12$ at a range of 200 m and varied with atmospheric conditions. The single-pulse S/N of the return signal from the hard target (brick wall) at a range of 1.1 km was ~ 130 .

A. Path-Averaged Water-Vapor DIAL Measurements

There are several absorption lines of water vapor within the tuning range of the Ho:YSGG laser that can be used for the differential absorption measurement of water vapor in the atmosphere. This may be seen in Fig. 3, where the computer-generated synthetic transmission spectrum of the atmosphere within the tuning range of the Ho:YSGG laser is shown.¹⁸ The three strong absorption lines in Fig. 3 are due to water vapor, whereas the other, weaker, lines are due to atmospheric CO_2 . Because the tuning range of Ho:YSGG is from 2.080 to $2.089 \text{ }\mu\text{m}$, the absorption line of water vapor near $2.0848 \text{ }\mu\text{m}$ (vacuum wave number 4796.554 cm^{-1}) may be used for DIAL measurements.

The backscattered lidar returns from a brick building at a range of 1.1 km were measured as the Ho-laser wavelength was tuned across the water-vapor absorption line near 4796.5 cm^{-1} . Figure 4 shows a plot of the normalized lidar returns obtained in 1 June 1990. As can be seen, the strong water-vapor absorption line is

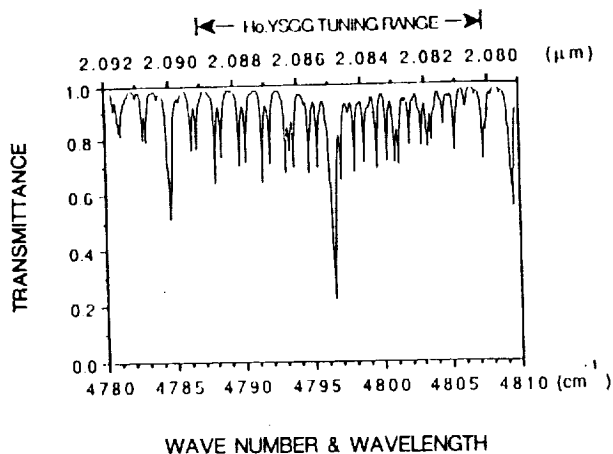


Fig. 3. Calculated atmospheric transmittance near the 2.084- μm wavelength region over a 10-km horizontal path showing overlap of the Ho:YSGG laser-tuning range. The three stronger absorption lines are due to water vapor, and the weak background absorption lines are due to CO_2 .

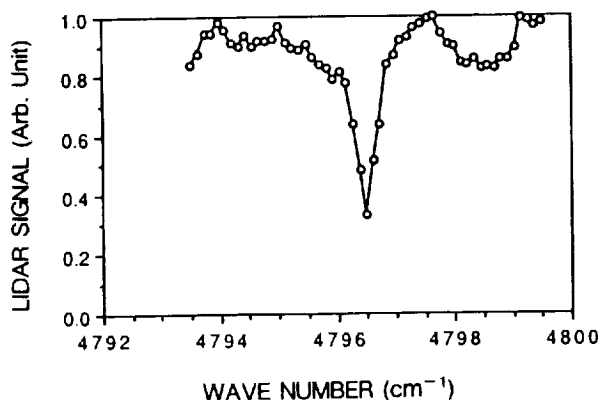


Fig. 4. Lidar returns backscattered from a building 1.1 km away as a function of the Ho:YSGG laser wavelength. The absorption line is due to water vapor in the atmosphere.

easily observed. The water-vapor absorption line near 4796.5 cm^{-1} has an absorption linewidth (FWHM) of $\sim 0.173\text{ cm}^{-1}$ and an absorption coefficient at line center of $4.70 \times 10^{-4}/\text{atm cm}$ at STP.^{19,20} The measured water-vapor absorption linewidth was estimated to be 0.25 cm^{-1} , which was obtained from the deconvolution of the Ho-laser linewidth (0.23 cm^{-1}) and the measured total linewidth (0.34 cm^{-1}) as shown in Fig. 4. It may be noted that the temperature dependence of the 4795.5 cm^{-1} water-vapor absorption line can be estimated from the published literature, which indicates that the coefficient for the temperature dependence of the air-broadened half-width is 0.64.^{19,20} For the experiments reported in this paper, this correction term was of the order of 3%, which is small compared with other uncertainties associated with our experiments. In addition, the temperature dependence of the Boltzmann population factor may be estimated from known theory, but previous water-vapor experiments have shown that direct absorption measurements are required if one is to quantify this factor

precisely.⁹ Thus the latter factor could not be taken into account in our experiments. However, future experiments with a multipass absorption cell are being planned to measure this value.

The concentration of water vapor in Fig. 4 was determined by using the Beer-Lambert law for attenuation, $I = I_0 \exp(-2\alpha NR)$, where I is the received power, I_0 is the incident power, α is the absorption coefficient, N is the concentration, and R is the range. By scaling the effective value of α by the ratio of the theoretical to the measured linewidths, the data shown in Fig. 4 indicate that ~ 13.2 Torr of water vapor was present in the atmosphere. This value may be compared with that obtained with a wet-dry bulb thermometer placed outside the window of the laboratory, which indicated 19.0 Torr of water vapor and an ambient temperature of 32.8°C . As is evident, the lidar-deduced value is less than that actually measured by $\sim 30\%$. This discrepancy most probably is due to errors caused by the laser linewidth's being comparable with the water-vapor absorption linewidth and, possibly, to variability in the spatial distribution of the water vapor. We are currently setting up a temperature-controlled, 1000-m-long multipass absorption cell to verify the water-vapor absorption coefficients and provide laboratory calibration of our DIAL measurements.

B. Range-Resolved Aerosol Backscatter-Water-Vapor DIAL Measurements

The Ho DIAL system was used to measure the range-resolved backscatter from naturally occurring aerosols in the atmosphere as the laser was tuned on, off-line through the water-vapor absorption line near $4796.5\text{ }\mu\text{m}$. To demonstrate the utility of the Ho DIAL system, we measured the variation of the atmospheric aerosol-water vapor as a function of time. The horizontal profiles of atmospheric aerosol backscatter and water-vapor concentration were obtained by pointing the lidar at approximately a $+2^\circ$ elevation angle and collecting 100-shot averaged return signals every 10 min. Each digitized signal was smoothed over a range interval of 30 m, and the aerosol backscatter and water-vapor concentration were calculated by using the lidar equation²¹ and the DIAL equation, respectively.²² The measured aerosol backscatter and water-vapor concentration horizontal profiles are shown in Figs. 5(a) and 5(b), respectively, as a function of time during the morning. The aerosol backscatter volume and water-vapor concentration are indicated by linear gray scales with dynamic ranges of 6 and 4, respectively. The overlap function and the aerosol attenuation were corrected experimentally for the lidar aerosol backscatter data by assuming that the aerosol density was homogeneous after 9 a.m.²³ It should be noted that this correction is a first-order approximation for the lidar aerosol backscatter, and a more rigorous technique, such as the Klett algorithm,²⁴ will be assessed for our future Ho lidar data. The DIAL measurement results, however, are not dependent on this correction technique.

As can be seen from Fig. 5(a), the atmospheric aero-

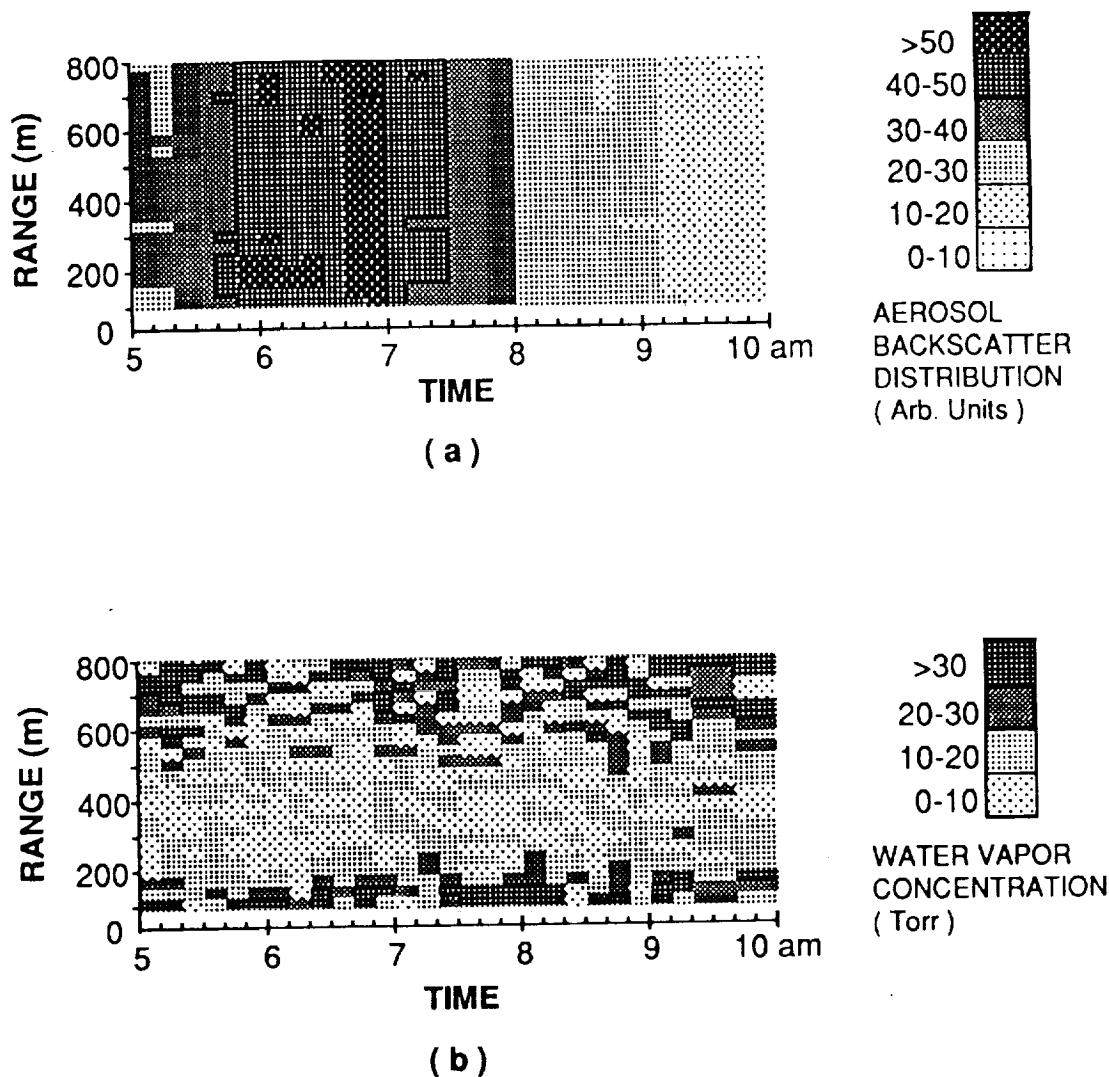


Fig. 5. Ho lidar/DIAL measurements of the temporal variation of (a) the atmospheric aerosol backscattering profile and (b) the atmospheric water-vapor concentration profile. The lidar was pointed at approximately a $+2^\circ$ elevation angle.

sol backscatter distribution was somewhat variable, especially during the morning sunrise (6:40 a.m.) and the associated increase in automobile traffic in the surrounding area. It should be noted that the range-resolved lidar signal shown in Fig. 5(b) is not so dramatic as that of our previous vertical aerosol-profile measurements⁵ because our present S/N is lower owing to the lower power of the tunable Ho laser and a more homogeneous distribution of atmospheric aerosol backscatter in the horizontal direction.

The water-vapor data shown in Fig. 5(a) show that the water-vapor density was somewhat constant in time and homogeneous over the first 200–700-m lidar range. The temperature was measured and varied from 24°C at 5 a.m. to 29°C at 10 a.m. The water-vapor concentration over the total path length was measured to be ~ 20 – 24 Torr. These lidar data essentially agree with those obtained by a wet-dry bulb thermometer measurement. However, we believe that in light of our large absolute error, as seen in the path-averaged measurement in Fig. 4, such close

agreement may be coincidental. Further lidar experiments are being conducted to quantify our results better and to reduce these errors.

IV. Summary and Future Work

In summary, we have developed a tunable, eye-safe Ho lidar-DIAL system, which has been used, for the first time to our knowledge, for the preliminary measurement of the atmospheric aerosol-backscatter and water-vapor concentration profiles. The Ho-lidar aerosol backscatter profile measurements indicate that detection of ~ 1 km can be achieved by using only 5–10-mJ/pulse laser pulse energy. The Ho DIAL experiments indicate that water-vapor concentration profile can also be obtained at such a range but with somewhat poor ($\sim 30\%$) accuracy.

Our plans are to evaluate the Ho lidar-DIAL system further by increasing the laser power and better controlling the laser linewidth and spectral purity. Recently several laser research groups have improved on the operation of the Ho laser, and their results have

shown (1) fixed single-frequency, narrow-linewidth operation, (2) high-power (1–10-J/pulse) operation in the non-Q-switched mode, and (3) moderate-power (350-mJ/pulse) operation in the Q-switched mode. We are currently upgrading our Ho laser to have higher-output power, of the order of 300 mJ, and to be injection locked to a single-frequency, tunable Ho oscillator. In this way, we hope to be able to quantify the performance of the Ho DIAL system better, especially in its spectroscopic utility for water-vapor measurements. Such quantitative measurements are required if one is to be able to compare directly the potential usefulness of the Ho DIAL system with current near-IR DIAL measurements of atmospheric water vapor.^{10,25,26}

This research was supported in part by the Florida High Technology and Industrial Council and by the NASA/Langley Research Center. When this research was performed, Sungdo Cha was a visiting scientist from the Department of Physics, Kangwon National University, Korea. The authors are grateful to the reviewers for several suggested improvements to this paper.

References

1. D. K. Killinger and N. Menyuk, "Laser remote sensing of the atmosphere," *Science* **235**, 37–45 (1987).
2. R. L. Byer, "Diode laser-pumped solid-state lasers," *Science* **239**, 742–747 (1988).
3. G. J. Quarles, A. Rosenbaum, C. L. Marquardt, and L. Esterowitz, "High-efficiency 2.09 μm flashlamp-pumped laser," *Appl. Phys. Lett.* **55**, 1062–1064 (1989).
4. M. J. Kavaya, S. W. Henderson, E. C. Russell, R. M. Huffaker, and R. G. Frehlich, "Monte Carlo computer simulations of ground-based and space-based coherent DIAL water vapor profiling," *Appl. Opt.* **28**, 840–851 (1989).
5. N. Sugimoto, N. Sims, K. Chan, and D. K. Killinger, "Eye-safe 2.1- μm Ho lidar for measuring atmospheric density profiles," *Opt. Lett.* **15**, 302–304 (1990).
6. P. W. Baker, "Atmospheric water vapor differential absorption measurements on vertical paths with a CO_2 lidar," *Appl. Opt.* **22**, 2257–2264 (1983).
7. R. M. Hardesty, "Coherent DIAL measurement of range-resolved water vapor concentration," *Appl. Opt.* **23**, 2545–2553 (1984).
8. W. B. Grant, J. S. Margolis, A. M. Brothers, and D. M. Tratt, " CO_2 DIAL measurements of water vapor," *Appl. Opt.* **26**, 3033–3042 (1987).
9. E. V. Browell, T. D. Wilkerson, and T. J. McIlrath, "Water vapor differential absorption lidar development and evaluation," *Appl. Opt.* **18**, 3474–3483 (1979).
10. G. Ehret and W. Renger, "Atmospheric aerosol and humidity profiling using an airborne DIAL system in the near IR," in *Digest of Topical Meeting on Optical Remote Sensing of the Atmosphere* (Optical Society of America, Washington, D.C., 1990), paper ThA6-1.
11. R. M. Schotland, in *Proceedings of the Fourth Symposium on Remote Sensing of the Environment* (Environmental Research Institute of Michigan, Ann Arbor, Mich., 1966), p. 273–283.
12. V. V. Zuev, V. E. Zuev, Yu. S. Makushikin, V. N. Marichev, and A. A. Mitsel, "Laser sounding of atmospheric humidity: experiment," *Appl. Opt.* **22**, 3742–3746 (1983).
13. N. Menyuk and D. K. Killinger, "Atmospheric remote sensing of water vapor, HCl and CH_4 using a continuously tunable CO:MgF_2 laser," *Appl. Opt.* **26**, 3061–3065 (1987).
14. L. F. Johnson, J. E. Geusic, and L. G. Van Uitert, "Coherent oscillation from Tm^{3+} , Ho^{3+} , Yb^{3+} and Er^{3+} ions in yttrium aluminum garnet," *Appl. Phys. Lett.* **7**, 127–129 (1965).
15. N. P. Barnes and D. J. Gettemy, "Pulsed Ho:YAG oscillator and amplifier," *IEEE J. Quantum Electron.* **QE-17**, 1303–1308 (1981).
16. S. W. Henderson and C. P. Hale, "Tunable single-longitudinal-mode diode pumped Tm:Ho:YAG laser," *Appl. Opt.* **29**, 1716–1718 (1990).
17. T. Y. Fan, G. Huber, R. L. Byer, and P. Mitzscherlich, "Spectroscopy and diode laser-pumped operation of Tm, Ho:YAG ," *IEEE J. Quantum Electron.* **24**, 924–933 (1988).
18. R. A. McClatchey and J. E. Selby, "Atmospheric attenuation of laser radiation from 0.76 to 31.25 μm ," *Environmental Research Paper 460* (U.S. Air Force Cambridge Research Laboratories, Bedford, Mass., 1974).
19. L. S. Rothman, R. R. Gamache, A. Goldman, L. R. Brown, R. A. Toth, H. M. Pickett, R. L. Poynter, J.-M. Flaud, C. Camy-Peyret, A. Barbe, N. Husson, C. P. Rinsland, and M. A. H. Smith, "The HITRAN database: 1986 edition," *Appl. Opt.* **26**, 4058–4097 (1987).
20. R. R. Gamache and R. W. Davies, "Theoretical calculations of N_2 -broadened halfwidths of H_2O using quantum fourier transform theory," *Appl. Opt.* **22**, 4013–4019 (1983).
21. R. T. H. Collis, "Lidar," *Appl. Opt.* **9**, 1782–1788 (1970).
22. R. M. Schotland, "Errors in the lidar measurement of atmospheric gases by differential absorption," *J. Appl. Meteorol.* **13**, 71–77 (1974).
23. Y. Sasano, H. Shimizu, N. Takeuchi, and M. Okuda, "Geometrical form factor in the laser radar equation: an experimental determination," *Appl. Opt.* **18**, 3908–3910 (1979).
24. J. D. Klett, "Stable analytical inversion solution for processing lidar returns," *Appl. Opt.* **20**, 211–220 (1981).
25. E. V. Browell, A. K. Goroch, T. D. Wilderson, and S. Ismail, "Airborne DIAL water vapor and aerosol measurements over the Gulf stream wall," presented at the 12th International Laser Radar Conference, Aix en Provence, France, 13–17 Aug., 1984.
26. E. V. Brownell, S. Ismail, and B. E. Grossmann, "Temperature sensitivity of differential absorption lidar measurements of water vapor in the 720-nm region," *Appl. Opt.* **30**, 1517–1524 (1991).

Heterodyne Doppler 1- μm lidar measurement of reduced effective telescope aperture due to atmospheric turbulence

Kin Pui Chan, Dennis K. Killinger, and Nobuo Sugimoto

We performed an experimental study on the effect of atmospheric turbulence on heterodyne and direct detection lidar at 1 μm , employing a pulsed Nd:YAG bistatic focused beam lidar that permitted simultaneous heterodyne and direct detection of the same lidar returns. The average carrier-to-noise ratio and statistical fluctuation level in the lidar return signals were measured in various experimental and atmospheric conditions. The results showed that atmospheric turbulence could reduce the effective receiver telescope diameter of the 1- μm heterodyne lidar to <5 cm at a relatively short range of ~ 450 m near the ground. The observed effective telescope aperture and heterodyne detection efficiency varied during the day as the atmospheric turbulence level changed. At this time, we are not able to compare our experimental lidar data to a rigorous atmospheric turbulence and lidar detection theory which includes independently variable transmitter, receiver, and detector geometry. It is interesting to note, however, that the observed limitation of the effective receiver aperture was similar in functional form with those predictions based on the heterodyne wavefront detection theory by D. L. Fried [Proc. IEEE 55, 57-67 (1967)] and the heterodyne lidar detection theory for a fixed monostatic system by S. F. Clifford and S. Wandzura [Appl. Opt. 20, 514-516 (1981)]. We have also applied such an effective receiver aperture limitation to predict the system performance for a heterodyne Ho lidar operating at 2 μm .

I. Introduction

Because of rapid progress in compact and tunable solid state lasers in recent years,¹ there has been increasing interest in the development of all solid-state lidar systems. While several demonstration systems of direct and heterodyne (coherent) lidar technology using solid state lasers at 1-2 μm have been reported,²⁻⁶ detailed studies of such lidar systems still lag far behind the extensive wealth of information known about the more common 10- μm CO₂ coherent lidar technology. The future development of solid state, coherent lidar is particularly significant for remote wind velocity and moving target measurements⁷ and will have a strong impact on satellite based, global wind measurements (such as the NASA/Lidar Atmospheric Wind Sounder) and aircraft windshear sensors for the FAA and NASA.

The extension of coherent Doppler lidar technology from 10- to the new 1-2- μm wavelength range will not only involve the development of new laser, detector, and optical systems, but will also involve detailed knowledge of the propagation characteristics of the lidar beam through the atmosphere. While there have been numerous past studies of lidar propagation in the turbulent atmosphere,⁸⁻²² a significant number of these studies were directed toward 10- μm CO₂ Doppler lidar measurements, with relatively few involved with experiments in the 1-2- μm wavelength range. Although the theoretical predictions can be scaled to a 1- or 2- μm wavelength range, experimental data are still required to validate these theoretical predictions.

In this paper, we report the first experimental study, to our knowledge, of the effect of atmospheric turbulence on heterodyne and direct detection of lidar signal returns at 1 μm . Measurements were made using a short-pulse (8-ns) coherent Nd:YAG bistatic focused beam lidar system, which also permitted simultaneous heterodyne and direct detection of the same lidar return radiation. The average carrier-to-noise ratio (CNR) and signal standard deviation were measured as a function of the receiver telescope aperture area. The effect of atmospheric turbulence was found to reduce severely the effective aperture size of the receiver telescope for a 1- μm heterodyne lidar.

Nobuo Sugimoto is with National Institute for Environmental Studies, Tsukuba 305, Japan; the other authors are with University of South Florida, Physics Department, Tampa, Florida 33620.

Received 19 July 1990.

0003-6935/91/182617-11\$05.00/0.

© 1991 Optical Society of America.

At this time we are not able to compare our experimental data to a rigorous atmospheric turbulence and lidar detection theory which includes independently variable transmitter, receiver, and detector geometry; since, to our knowledge, no such general theory exists in the published literature. However, it was found that the observed limitation of effective receiver aperture area was similar in functional form to the related atmospheric turbulence predictions based on the distorted wavefront detection theory by Fried¹² and the heterodyne lidar detection theory for a fixed monostatic system by Clifford and Wandzura.¹⁹ These results quantify the effective receiver aperture area for heterodyne detection at 1 and 2 μm and provide a comparison of the CNRs achieved with heterodyne and direct detection technique. It should be emphasized that our experimental lidar data were obtained for the lidar propagation along a horizontal path, and the laser beam was focused on the target. We plan to study the more general case of a collimated or infinity-focused beam lidar in the immediate future and hope to be able to compare these results to future theoretical analysis. In addition, the more practical case of a slant-path (variable altitude) lidar will also be studied.

The organization of our paper starts in Sec. II with a brief summary of the theories derived by other researchers for optical heterodyne detection in the presence of atmospheric turbulence, to introduce the appropriate parameters. Section III presents the experimental setup and the measured average CNR and standard deviation of the fluctuating lidar signal returns. In Sec. IV, the experimental results are compared to the related theories given by Fried and Clifford/Wandzura and are shown to be similar in functional form. The parameter values determined from the experiments are then used in an analytical treatment to provide an estimate of the system performance for a 1- μm Nd and 2- μm Ho lidar operating in different conditions. Finally, Sec. V gives the conclusion.

II. Related Atmospheric Turbulence and Heterodyne Lidar Detection Theory

In this section we give a brief summary of the performance estimation for heterodyne detection in terms of the CNR with an emphasis on the measurement of lidar propagation through the turbulent atmosphere. This summary is based on previous work by others and aims to help explain the terminology used and to outline some of the previous theoretical works which have a bearing on the present experimental work.

In the heterodyne detection system to be discussed, it is assumed that the lidar return radiation collected by the receiver telescope is collimated, mixed with the local oscillator radiation, and focused onto a photodiode. In the absence of atmospheric turbulence and target speckles, it is assumed that the amplitude and phase of the signal electrical field, E_{s0} , and ϕ_s , are uniform on the receiver aperture plane. As such, the time-averaged output of the square-law detector at the intermediate frequency i_{if}^2 , can be given by

$$i_{if}^2 = \langle i_{if}^2 \rangle + \langle i_{if}^2 \rangle^2 \quad (1)$$

where Ω is the receiving efficiency of a coherent lidar system which has been recently shown to be $\sim 0-0.4$ for a monostatic lidar,²³ η is the quantum efficiency of the detector which is assumed to be uniform over the detector area, e is the charge of the electron, $h\nu$ is the photon energy, $A_r = \pi d_r^2/4$ is the receiver aperture area, d_r is the receiver telescope diameter, and E_{lo} is the amplitude of the local oscillator radiation which, for simplicity, is assumed to be uniform on the detector plane. In shot-noise dominated heterodyne detection, the rms noise current of the square-law detector can be approximated by²⁴

$$\langle i_{if}^2 \rangle = 2eB(\eta e P_l / h\nu), \quad (2)$$

where $P_l = A_r E_{lo}^2/2$ is the collected intensity of the local oscillator, and B is the electrical bandwidth of the detector amplifier. From Eqs. (1) and (2), the CNR for heterodyne detection in the absence of atmospheric turbulence and target speckles $\text{CNR}_{H,0}$ is given by

$$\text{CNR}_{H,0} = \overline{i_{if}^2} / \langle i_{if}^2 \rangle = \Omega \eta P_s / (h\nu B), \quad (3)$$

where $P_s = A_r E_{s0}^2/2$ is the collected signal intensity. It is seen from Eq. (3) that the CNR for heterodyne detection of a nondistorted signal wavefront is proportional to the receiver aperture area A_r .

In the presence of atmospheric refractive turbulence, the wavefront of the lidar signal is distorted while propagating in the atmosphere. The combined effect of atmospheric turbulence on heterodyne lidar detection may be described approximately by a parameter ρ_0 called the atmospheric turbulence field coherence length, which can be given by^{8,20}

$$\rho_0 = \left[2.91 k^2 \int_0^R C_n^2(z) (1 - z/R)^{5/3} dz \right]^{-3/5}, \quad (4)$$

where k is the wavenumber, C_n^2 is the refractive index structure parameter of the atmosphere, and R is the detection range.

Fried previously developed an analytical model for the heterodyne detection of such an atmospherically distorted wavefront,¹² in which the extent of the wavefront distortion was characterized using only a given value of ρ_0 . His analytical results pointed out that the ensemble average of the time-averaged output of the square-law detector $\langle i_{if}^2 \rangle$ should be given in the form of Eq. (1) but multiplied by a factor $F_0(U)$ given as

$$F_0(U) = (16/\pi) \int_0^1 u [\cos^{-1} u - u(1-u^2)^{1/2}] \times \exp[-(1/2)(Uu)^{5/3}] du, \quad (5)$$

where $U = d_r/\rho_0$. Equation (5) is essentially Eq. (5.16) in Fried's paper¹² but has been slightly modified to use the definition of ρ_0 as used in Refs. 8 and 20. The average CNR for heterodyne detection in the presence of atmospheric turbulence $\text{CNR}_{H,av}$ is thus given by

$$\text{CNR}_{H,av}(d_r, \rho_0) = \langle i_{if}^2 \rangle / \langle i_{if}^2 \rangle = \text{CNR}_{H,0} F_0(U). \quad (6)$$

It should be pointed out that Eq. (5) was derived using

Fried's model which includes a first-order estimation of optical heterodyne detection and the effect of atmospheric turbulence in the form of the magnitude of ρ_0 , but with no specific consideration on the propagation of the transmitted and backscattered laser light and their effects on the determination of the value of ρ_0 . As can be seen in Eq. (6), $F_0(U)$ is essentially a factor describing the reduction in the average CNR from the effects of atmospheric turbulence. By examining Eqs. (5) and (6), we see that for $U \ll 1$ (i.e., $d_r \ll \rho_0$), $F_0 \cong 1$ and $\text{CNR}_{H,av} \cong \text{CNR}_{H,0}$. In this case, there is little effect from atmospheric turbulence. On the other hand, for $U \gg 1$ (i.e., $d_r \gg \rho_0$), $F_0 \cong (3\rho_0/d_r)^2$ and $\text{CNR}_{H,av} \cong \text{CNR}_{H,0}(3\rho_0/d_r)^2$. Noting that $\text{CNR}_{H,0}$ is proportional to $A_r = \pi d_r^2/4$, $\text{CNR}_{H,av}$ is readily seen to be proportional to $(3\rho_0)^2$. This indicates that the CNR of heterodyne lidar detection may not depend on the aperture size of the receiver telescope but may be limited by the atmospheric coherence length ρ_0 on the receiver aperture plane.

Clifford and Wandzura have calculated CNR reduction factor F_0 for a fixed geometry, monostatic heterodyne lidar but in addition took into account the correlation effect of the forward and backward lidar propagation through the same atmospheric turbulence.¹⁹ Their results found that for lidar measurements where the laser beam is focused on the target

$$F_0(U) \cong [1 + (U/3)^2]^{-1}, \quad (7)$$

where $U = d_r/\rho_0$ is the same as in Eqs. (5) and (6). It may be noted that in the original work of Clifford and Wandzura,¹⁹ F_0 was given by $F_0 \cong [1 + (d_r/2\rho_0)^2]^{-1}$. We have replaced this with the current form in Eq. (7) because the value of ρ_0 used by Clifford and Wandzura is larger by a factor of ~ 1.5 than that used in this paper. It is also seen in Eq. (7) that for $U \gg 1$, $F_0 \cong (3\rho_0/d_r)^2$, so that $\text{CNR}_{H,av}$ is limited by the magnitude of ρ_0 , a similar result as that given in Eq. (5).

To summarize, the above theoretical studies of Fried and Clifford/Wandzura give physical insight into some of the processes occurring in a lidar experiment. Fried's analysis does not aim to predict a value of ρ_0 (or of C_n^2) but states that if a value for ρ_0 has been measured or assumed, its effect on the heterodyne detection efficiency is given as in Eq. (5). The analysis of Clifford/Wandzura calculates the influence of C_n^2 on a monostatic lidar system and predicts a heterodyne

detection efficiency reduction factor which is approximated by Eq. (7) for a focused transmitter beam. In general, however, there are no published theoretical analyses on the detection efficiency of a bistatic or monostatic heterodyne lidar which allows the practical (i.e., experimental) freedom to vary independently the size of the transmitter, receiver, and detector. What is required for the lidar system design is such a theory which would be able to predict the ρ_0 value on the telescope pupil plane of a bistatic or monostatic lidar system and its overall effect on the heterodyne detection efficiency. Several research groups are now working on these theories, and we hope to be able to directly compare our experimental work with them when they become available. Until this time, however, we believe that comparison of our experimental data to the related theories of Fried and Clifford/Wandzura, while not exact, will give insight into the physics involved.

III. Experiment

Our lidar experiments were carried out employing a short pulse, heterodyne Doppler Nd:YAG lidar at $1.06 \mu\text{m}$, which has been described in detail in a separate paper.⁶ Figure 1 is a schematic of the lidar system. The transmitter laser was an injection-seeded, Q-switched Nd:YAG laser with a pulse output energy of $\sim 100 \text{ mJ}$ and a pulse length of $\sim 8 \text{ ns}$. The laser beam size was measured to be $\sim 6 \text{ mm}$ at the $\exp(-2)$ point of its maximum intensity. About 98% of the laser pulse energy was attenuated before the laser beam was expanded sixteen times and transmitted to the distant target by a 13-cm diam Newtonian telescope. The transmitted laser radiation was focused on the distant target. Backscattered laser radiation was collected using a Cassegrainian telescope with a full aperture diameter of 40 cm and an effective focal length of 5 m. The two telescopes were put close to each other with a separation of $\sim 25 \text{ cm}$ between optic axis and aimed at the same target.

In the present experiments, the receiver aperture diameter was made variable over a range of 5–20 cm, to study the effects of the aperture size on heterodyne and direct detection. After collimation with a lens whose focal length was 10 cm, the signal beam was attenuated with ND filters and split into two beams with a 50/50 beam splitter; the diameter of the signal beam was $\sim 1\text{--}4 \text{ mm}$, corresponding to the receiver

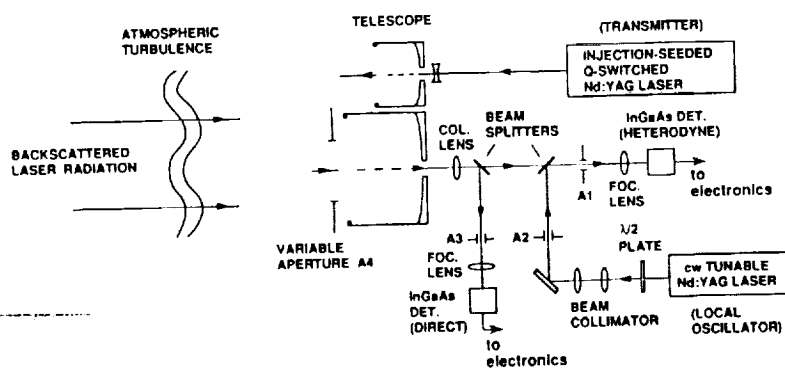


Fig. 1. Schematic of short-pulse Nd:YAG lidar system at $1 \mu\text{m}$ providing simultaneous heterodyne and direct detection of the same lidar return.

telescope diameter of 5–20 cm. One of the signal beams was focused and directly detected by an InGaAs PIN detector, and the other was mixed with the Nd:YAG local oscillator output, focused, and heterodyne detected by another InGaAs PIN detector. The two detectors used for heterodyne and direct detection detectors were identical, both with a 100- μm diameter and a rise time shorter than 0.5 ns. The focal length of the focusing lens was chosen to be 4 cm for both heterodyne and direct detection detectors, so that the diffraction-limited focal spot size (i.e., $\sim 25\text{--}100\ \mu\text{m}$ with respect to the 5–20-cm receiver diameter) could be equal or less than the detector diameter. The diameter of the local oscillator output was measured to be $\sim 1\ \text{mm}$ at the $\exp(-2)$ point of its maximum intensity. In the heterodyne lidar measurements, it was collimated/expanded by using either a 2 \times or a 4 \times beam expander to help match the $\sim 1\text{--}4\text{-mm}$ diameter of the lidar signal beam.

By frequency tuning the laser diode pumped cw Nd:YAG local oscillator, the intermediate frequency of the heterodyne signal was variable over a range of 200 MHz to 1 GHz. The maximum output power of the local oscillator was 4 mW. The detector output was amplified using a low noise, wide bandwidth preamplifier with a 26-dB gain, passed through a 200-MHz high pass filter, full-wave rectified using a microwave detector with appropriate capacitor and amplified 100 \times before being digitized with a high-speed, twelve-channel, analog-to-digital (A-D) converter in a CAMAC/computer system. Since no square-law detector was used, the digitized heterodyne signal was squared prior to data processing in the computer to be directly comparable to standard heterodyne detection theory.²⁴ The output of the direct detection detector/amplifier was digitized with the A-D converter as well. The lidar system was operated at a 10-Hz repetition rate, and the computerized data acquisition and processing were performed in real time.

The laser beam was transmitted from the lidar system stationed on the third floor of our laboratory building and focused onto a brick wall $\sim 450\ \text{m}$ away and 10 m above the ground. The focused beam size was measured to be $\sim 1\ \text{cm}$. Figure 2 shows an example of a single pulse, heterodyne detection lidar return as displayed/recorded on a fast 1-GHz oscilloscope. As can be seen, the lidar signal consists of the 550-MHz heterodyne signal superimposed on top of the 8-ns long, direct detection envelope signal. What is also shown in Fig. 2 is an example of how the receiver aperture size affects the heterodyne detection CNR. In Fig. 2(a) where receiver aperture diameter d_r was 5 cm, the oscillatory heterodyne signal is much stronger than the direct detection (envelope) signal. On the other hand, in Fig. 2(b), where $d_r = 15\ \text{cm}$, almost equal heterodyne and direct signal intensity were observed.

A. Effect of Telescope Aperture Size on CNR

To measure experimentally the effect of the receiver telescope aperture size on the lidar CNR values, the average lidar CNR for both heterodyne and direct

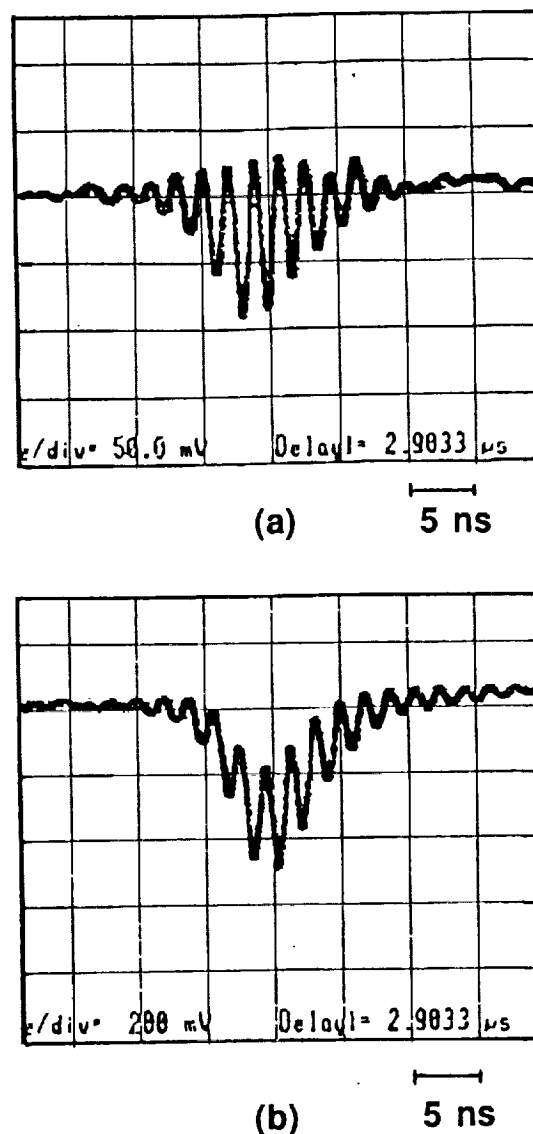


Fig. 2. Oscilloscope displays showing a single-pulse heterodyne signal of lidar return from a hard target at a range of 450 m. The receiver telescope aperture size was (a) 5 and (b) 15 cm. Note that the 550-MHz heterodyne signal is superimposed on top of the direct detection, 8-ns long pulse envelope.

detection techniques was measured as a function of the receiver aperture area. Figure 3(a) shows an example of our data obtained when the aperture diameter of the aperture stop placed in front of the receiver telescope (i.e., A4 in Fig. 1) was changed from 5 to 20 cm. The measurement was made at noon on a sunny day in Jan. 1990 (temperature $\sim 20^\circ\text{C}$). Each data point shown was an average of 600 returned pulses, and the whole experiment was carried out in about half an hour. In this experiment, the diameter of the collimated local oscillator beam was matched to that of the signal by varying the diameter of aperture A2 placed in front of the local oscillator. The collection apertures in front of the detectors (A1 and A3) were fully open and essentially not used.

As seen in Fig. 3(a), the intensity of the direct detec-

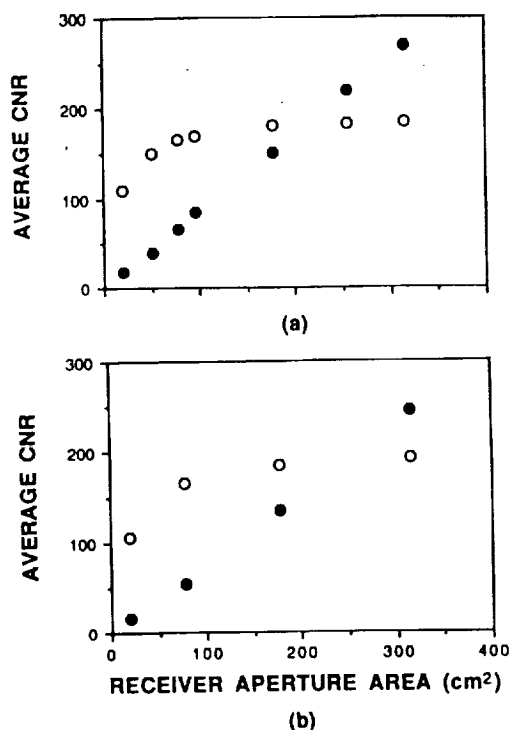


Fig. 3. Measured average CNR for heterodyne (open circles) and direct detection (solid circles) of lidar returns from a hard target at a range of 450 m as a function of the receiver aperture area, which was varied by changing the diameter of (a) the receiver telescope aperture and (b) the collection aperture stops in front of the heterodyne and direct detection detector.

tion signal increased in proportion to the telescope aperture area due to the effect of aperture speckle averaging.²⁵ However, the heterodyne signal intensity is seen in Fig. 3(a) to initially increase in proportion to the telescope aperture area but then saturates to a maximum value. This maximum value was observed to change in time by as much as a factor of ~ 2 – 3 during the day, presumably the result of the changes in the level of atmospheric turbulence; this is discussed below. In the data shown in Fig. 3(a), little improvement in CNR was made by increasing the receiver aperture size larger than ~ 10 cm. It should be also added that despite the complex detection procedure, heterodyne detection did not offer superior performance in terms of the CNR compared with the straightforward direct detection because of the small value of the effective receiver aperture size and the wide electrical bandwidth (1 GHz) of our lidar system.

We also performed a similar experiment but changed the diameters of the apertures in front of the detectors (A1 and A3), instead of the aperture in front of the telescope. This was done to mimic the conditions assumed for several atmospheric turbulence theories which take into account a variable aperture stop in front of the detector and then backward propagate the local oscillator radiation to the target through the telescope. Figure 3(b) shows our experimental lidar data, which was obtained by varying the diameter of the collection apertures placed in front of the detectors

(A1 and A3) d_c over the range of 1–4 mm and leaving A2 and A4 fully open. The equivalent receiver telescope aperture area A_r was estimated from $A_r = \pi(f_r d_c / 2f_l)^2$ where f_r and f_l are the focal length of the receiver telescope and the collimating lens, respectively. As can be seen, the results shown are essentially the same as those presented in Fig. 3(a).

During the course of the above experiments, we were able to measure an approximate value of the level of the atmospheric turbulence using a new instrument which acquires the 2-D Fourier transform/power spectrum of the telescope image of a distant light source, recorded by using a video camera.²⁶ Our measurement indicated that the value of C_n^2 varied during the course of our lidar experiment from ~ 2 to $7 \times 10^{-14} \text{ m}^{-2/3}$ at 10 m above the ground (horizontal path, temperature range from 18 to 24°C, sunny day). From the approximation of $C_n^2(h) = C_n^2(1)h^{-4/3}$, where $C_n^2(1)$ is the value at $h = 1$ -m height,²⁷ we estimate a corresponding value for $C_n^2(1)$ of $\sim 4 \times 10^{-13}$ to $1.4 \times 10^{-12} \text{ m}^{-2/3}$ during the day. We are currently in the process of comparing the C_n^2 value measured with our video camera instrument with that measured with a conventional scintillometer recently obtained on loan for NOAA. In this way, a better quantitative value for C_n^2 can be obtained. [Note added in Proof: We have recently been able to use the NOAA C_n^2 scintillometer in our experiments and have found a good agreement (within 30%) of the C_n^2 value measured with our video camera system.]

B. Effect of Telescope Aperture Size on Signal Fluctuations

The statistical fluctuation level of the lidar signal intensity was measured for both the heterodyne and direct detection techniques. Figure 4 shows the normalized standard deviations of the lidar signal returns shown in Fig. 3(a). As seen, the differences between the results measured with the two detection techniques are evident. The normalized signal standard deviation (σ) for heterodyne detection did not appear to depend on the receiver aperture area in our experimental conditions and had a value of around 1.1. This observed value is slightly larger than unity, which is expected for the familiar Rayleigh distribution associated with heterodyne detection.²⁵ On the other hand, the value of σ for direct detection measurement is seen to decrease as the telescope aperture area is increased. This is, as expected, the result of aperture speckle averaging.²⁵

The value of σ in Fig. 4 can be compared to previous reports by Holmes *et al.*^{15,18} In their works, the signal covariance σ^2 for a nonfocused point receiver (direct detection) was found to approach a maximum value of about 1.3, when the Rytov logarithm amplitude variance $\sigma_x^2 = 0.124C_n^2 k^{7/6} R^{11/6}$ was nearly 0.1. Using typical values for our experiment of $R = 450$ m, $\lambda = 1.06 \mu\text{m}$, and $C_n^2 = 7 \times 10^{-14} \text{ m}^{-2/3}$, one calculates that $\sigma_x^2 = 0.05$. From Fig. 1 of Ref. 18, the predicted value of σ corresponding to $\sigma_x^2 = 0.05$ is ~ 1.1 . This value is in good agreement with our heterodyne lidar data shown in

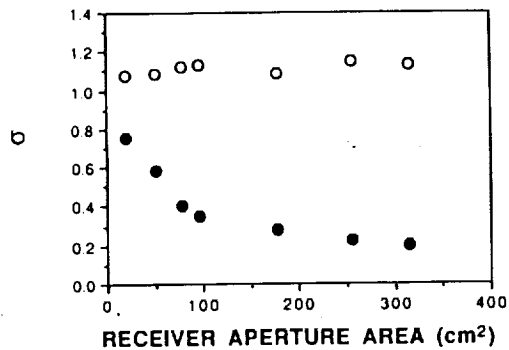


Fig. 4. Measured normalized signal standard deviation of heterodyne (open circles) and direct detection (solid circles) lidar returns from a hard target at a range of 450 m as a function of the receiver telescope aperture area.

Fig. 4. In this case, we are comparing our heterodyne lidar data to that of a specific direct detection measurement that employed a nonfocused point receiver, because both detection processes are essentially similar in detecting an interference (i.e., speckle) pattern. On the other hand, our direct detection lidar data shown in Fig. 4 also indicate that the value of σ may approach 1.0 for a point receiver (nearly zero aperture area). As can be seen, our values for σ are consistent with the study of Holmes *et al.*

The reduction in signal fluctuation observed for our 1- μm direct detection lidar in Fig. 4 may be contrasted with that normally expected using a 10- μm CO₂ lidar. From Eq. (4) it can be calculated that at $\lambda = 1.06 \mu\text{m}$, ρ_0 is $\sim 1.4 \text{ cm}$, assuming that the atmospheric parameter $C_n^2 = 7 \times 10^{-14} \text{ m}^{-2/3}$ is uniform along the 450-m long lidar propagation length. In the same atmospheric conditions, the predicted ρ_0 at $\lambda = 10 \mu\text{m}$ is $\sim 22 \text{ cm}$. Because of the smaller atmospheric speckle size at 1 μm , aperture speckle averaging is more effective for direct detection of Nd:YAG lidar returns than at 10 μm . For example, a normalized signal standard deviation as low as 0.2 was observed in our 1- μm lidar measurement at a detection range of 450 m, while a similar value for σ was measured with a 10- μm CO₂ lidar at a much longer (3 km) range.²⁸

C. Temporal Changes of Lidar CNR and Signal Fluctuation During the Day

It is instructive to show the differences in performance between the heterodyne and direct detection techniques in different atmospheric conditions. Figures 5(a) and (b) depict the average CNR and normalized signal standard deviation of the hard-target lidar returns, recorded between 6:30 a.m. and 12:00 a.m. on 5 Feb. 1990. The weather condition was sunny, and the temperature varied from 18 to 23°C. The detection range was $\sim 450 \text{ m}$, and the receiver telescope diameter was always fixed at 8 cm. Each data point shown is the average of 600 lidar returned pulses. In the present experimental conditions, the receiver aperture diameter was several times larger than the value of ρ_0 , which was estimated to vary around 1–3 cm. As seen in Fig. 5(a), a CNR value of ~ 200 was measured with heterodyne detection at 6:30 a.m. when the atmosphere was

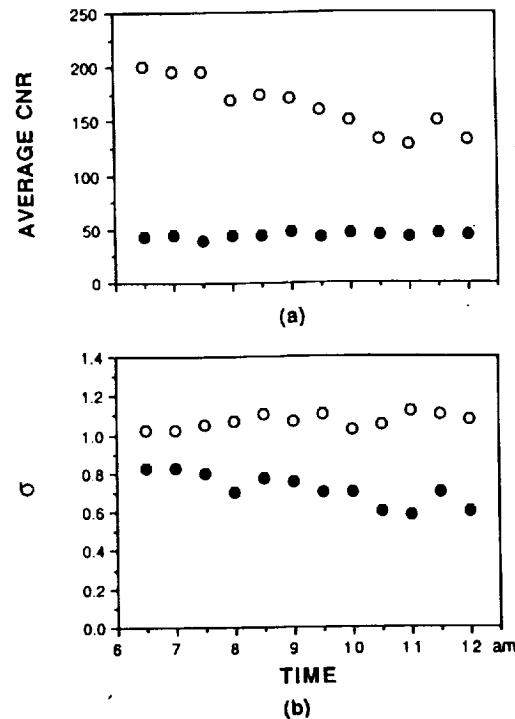


Fig. 5. Measured variation of (a) average CNR and (b) normalized signal standard deviation of heterodyne (open circles) and direct detection (solid circles) lidar returns from a hard target at a range of 450 m as a function of time during the day.

relatively calm. It dropped to ~ 120 at noon when the atmosphere became most turbulent. On the other hand, the signal intensity measured with direct detection was nearly constant during this time period. As seen in these experimental results, the heterodyne detection efficiency is degraded by the presence of atmospheric turbulence, and this effect changes in time as the level of atmospheric turbulence varies during the day.

The result shown in Fig. 5(b) is quite similar to that shown in Fig. 4. The normalized signal standard deviation of the direct detection was measured as ~ 0.8 when the atmosphere was relatively calm and ~ 0.6 at noon when the atmosphere was most turbulent. The value for σ may be approximated by $\sigma = 1/M^{1/2}$, where M is the ratio of the receiver aperture area to the speckle pattern correlation area,²⁶ which, in the present experiment where the laser beam was focused on the target, is essentially the number of atmospherically induced speckles on the receiver aperture plane. As such, the observed differences in σ value are believed to be the result of the nearly 30% change in the value of ρ_0 during this time period.

IV. Analysis and Discussion

A. Comparison of Experimental Lidar CNR to Related Atmospheric Turbulence and Lidar Detection Theory

At this time, it is not possible to compare our heterodyne lidar data to a rigorous atmospheric turbulence-lidar detection theory which allows the freedom to vary independently of the parameters of the transmitter,

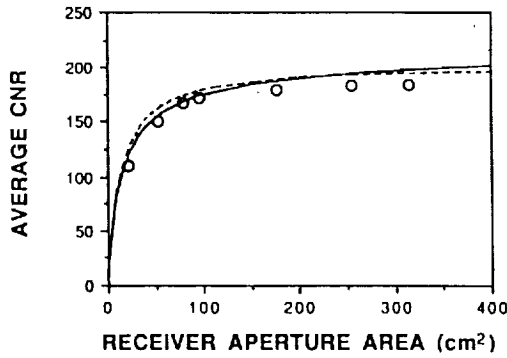


Fig. 6. Comparison of measured lidar CNR values (open circles) and theoretical predictions using the theories presented by Fried¹² (solid line), and Clifford and Wandzura¹⁹ (dashed line).

receiver, and detector diameter of a bistatic lidar system. However, it is shown in this section that our experimental data follow closely the functional form of the related theories by Fried and Clifford/Wandzura.

The theoretical average CNR for heterodyne detection can be calculated employing Eq. (6), using Eq. (3) to obtain $CNR_{H,0}$, and Eqs. (5) and (7) to obtain F_0 . In Eq. (3), the intensity of the lidar signal backscattered from the hard target P_s may be approximated by

$$P_s = [P_t \zeta A_r K \exp(-2\alpha R)]/R^2, \quad (8)$$

where P_t is the transmitted laser power, ζ is the target reflectivity, A_r is the receiver telescope aperture area, K is the overall optical efficiency, α is the absorption coefficient of the atmosphere, and R is the lidar detection range.

Using the parameter values for our lidar experiments, the theoretical CNR values were calculated and are shown in Fig. 6. In Fig. 6, the solid line was calculated using Eq. (5) given by Fried, the dotted line used Eq. (7) given by Clifford and Wandzura, and the open circles are our experimental data as repeated from Fig. 3(a). In these calculations, the estimated values for our lidar experimental parameters were: $P_t = 5 \text{ mJ}/8 \text{ ns} = 6 \times 10^5 \text{ W}$, $\zeta = 0.1$, $K = 0.1 \times 0.02$ (0.02 due to 98% signal attenuation with ND filters), $\exp(-2\alpha L) = 0.9$, $R = 450 \text{ m}$, $\eta = 0.8$, $h\nu = 1.86 \times 10^{-19} \text{ J}$, $B = 500 \text{ MHz}$, and $C_n^2 = 7 \times 10^{-14} \text{ m}^{-2/3}$. For the case of heterodyne detection, we estimate that the optical detection efficiency is further reduced by a factor of G , which is the result of the mismatch in optical alignment (geometrical form, wavefront, polarization, etc.)^{29,30} and the heterodyne receiving efficiency Ω .²³ In the experimental data shown in Fig. 6, G was estimated to be $\sim 3.5\%$ by comparing the experimental CNR with the theoretical predictions.

As seen in Fig. 6, the experimental data are similar in functional form with the related theoretical predictions, where $\rho_0 = 1.4 \text{ cm}$ was assumed for our experimental conditions ($C_n^2 \cong 7 \times 10^{-14} \text{ m}^{-2/3}$ and $R \cong 450 \text{ m}$). It is also noteworthy that although Eq. (7) was derived for a focused beam, monostatic lidar, very close agreement was observed with this prediction and our experimental data measured with a focused beam, bistatic lidar system. This may be partially explained

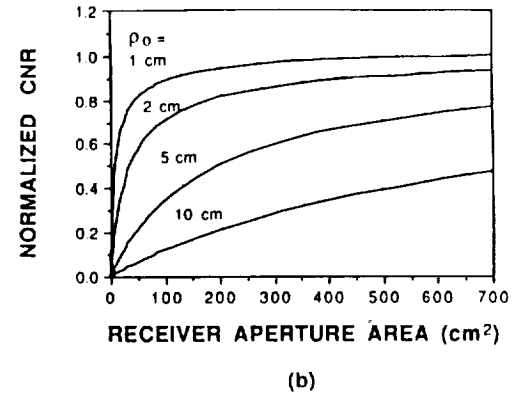
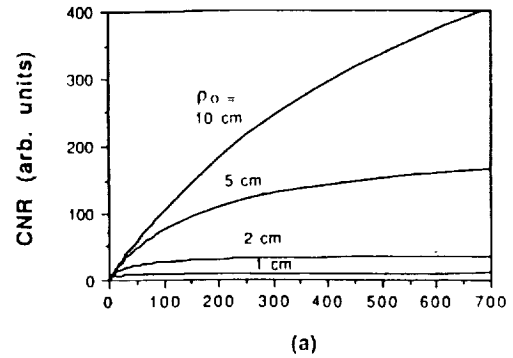


Fig. 7. Calculated results of (a) heterodyne lidar detection CNR in the presence of atmospheric turbulence and (b) the normalized value to the maximum CNR that a heterodyne lidar achieves with an effective receiver telescope aperture area of $A_{\text{eff}} = \pi(3\rho_0)^2/4$. The receiver telescope is varied over a range of 0–700 cm², i.e., telescope diameter of 0–30 cm.

by the fact that Eq. (7) is an approximated form of a more rigorous equation and is accurate within 20%.¹⁹ In addition, in our bistatic lidar system the separation of the transmitter and receiver telescope optic axis was 25 cm, so that there could still be partial correlation of the forward and backward lidar propagation. However, a more rigorous analysis as well as further experimental investigation is required to better quantify these results.

To compare the CNR for direct detection, we assume that the dominant noise sources are the detector dark current and amplifier noises. In this case, the voltage CNR for direct detection can be approximated by

$$CNR_D = P_s / (NEP_{DL}^2 + NEP_{AL}^2)^{1/2}, \quad (9)$$

where $NEP_{DL} = (h\nu/\eta)(2I_D B/e)^{1/2}$ and $NEP_{AL} = (h\nu/\eta)(2I_E B/e)^{1/2}$ are the noise equivalent powers of the detector and amplifier, respectively, I_D is the detector dark current, and I_E is the amplifier noise current.²⁴ Using the estimated values for our detection system of $NEP_{DL} = 4 \times 10^{-9} \text{ W}$, and $NEP_{AL} = 3 \times 10^{-8} \text{ W}$, the calculated CNR_D is found to be ~ 90 for a receiver telescope with $d_r = 8 \text{ cm}$, which is larger than the measured value $CNR_D \cong 45$ by a factor of 2.

Finally, it should be noted that the fitting of the theoretical curves in Fig. 6 to our experimental lidar

data was made by adjusting only one parameter, which was the value of ρ_0 . To illustrate this functional dependence of CNR on ρ_0 , Fig. 7(a) shows the numerical prediction of the heterodyne lidar detection CNR in the presence of atmospheric turbulence, using the heterodyne wavefront detection theory by Fried [i.e., Eq. (5)]. In Fig. 7, the receiver telescope aperture area was varied over a range of 0–700 cm² (i.e., $d_r = 0$ –30 cm) and four values of ρ_0 (1, 2, 5, and 10 cm) were chosen to represent different levels of atmospheric turbulence. As seen in Fig. 7(a), the value of ρ_0 dramatically changes the saturated value of CNR at aperture sizes much larger than ρ_0 . The maximum value for CNR is proportional to ρ_0^2 , which is explained in the next section.

Figure 7(b) shows similar data, but the values of CNR have been normalized to the maximum value CNR_{max} obtained at very large aperture size. As seen in these calculated results, the functional curve fitting of ρ_0 to CNR is quite sensitive and appears to yield a unique value of ρ_0 with a small relative error. While the calculated maximum CNR can be fitted to the experimental result by using the scale factor G , the shape of the curve is not changed by the magnitude of G but determined solely by ρ_0 .

B. Predicted Effective Receiver Telescope Aperture for 1- μ m Coherent Lidar

Thus far it has been experimentally shown that heterodyne detection efficiency can be severely degraded by atmospheric turbulence and is related to the reduction in the effective receiver aperture for a coherent lidar system. Here effective receiver aperture area A_{eff} is defined to be equivalent to an aperture area on which the signal wavefront is uniform, so that Eq. (3) is directly applicable for calculating the lidar CNR value. It is readily shown from Eqs. (3) and (6) that A_{eff} is given by

$$A_{eff} = F_0(U)A_r, \quad (10)$$

where $A_r = \pi d_r^2/4$ is the receiver telescope aperture area. Equation (10) is valid only when the target speckle size is much larger than the value of ρ_0 , so that the target speckle effects are negligible. As shown in Sec. II, for a receiver telescope whose aperture size is far larger than ρ_0 , $F_0(U)$ approaches $(3\rho_0/d_r)^2$. As a result, the maximum value of A_{eff} will be $A_{eff,max} = \pi(3\rho_0)^2/4$, i.e., a receiver telescope with a maximum effective aperture size of $d_{eff,max} = 3\rho_0$. In our experiments where ρ_0 was typically measured to be ~ 1.4 cm, $d_{eff,max} \cong 4$ cm.

Determining the optimal receiver telescope size for a heterodyne Doppler lidar is a very practical question. As a design method, the useful diameter of the receiver telescope d_r may be determined by the following equation:

$$\text{CNR}_{H,\Psi}(d_r, \rho_0) = \Psi \text{CNR}_{H,\Psi}(d_r \rightarrow \infty), \quad (11)$$

where Ψ is a factor that gives the CNR value of the lidar system as a fraction of its maximum CNR value. To illustrate the use of Eq. (11), we take three examples of

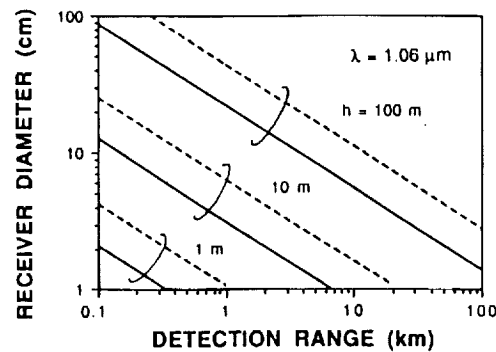


Fig. 8. Calculated results of the maximum effective receiver telescope diameter (solid lines) and the practically useful telescope diameter (dashed lines) for a 1.06- μ m Nd:YAG heterodyne lidar as a function of detection range. The atmospheric parameters $C_n^2 = 1 \times 10^{-12}$, 5×10^{-14} , and $2 \times 10^{-15} \text{ m}^{-2/3}$ are assumed to be uniform along the horizontal lidar propagation path at a height of 1, 10, and 100 m, respectively.

$\Psi = 70, 80, \text{ and } 90\%$. Substituting Eqs. (3), (5), and (6) into Eq. (11) yields the numerical solution of $d_r \cong 5\rho_0, 6\rho_0, \text{ and } 9\rho_0$ for $\Psi = 70, 80, \text{ and } 90\%$, respectively. This result shows that it may not be practical to use a receiver telescope whose diameter is much larger than $6\rho_0$, since no significant improvement will be made by increasing d_r beyond this value. As can be seen, the above result is consistent with the experimental data and theoretical predictions shown in Figs. 6 and 7. It may also be noted that the numerical solution of Eq. (11) using Eq. (7) yields nearly the same results.

The maximum effective receiver telescope diameter for a 1.06- μ m Nd:YAG heterodyne lidar with $d_r = 3\rho_0$ was calculated using Eq. (4) as a function of the detection range, and the results are shown in Fig. 8 (solid lines). For references, the calculated results of the practically useful telescope diameter $d_r = 6\rho_0$, is also shown (dashed lines). In Fig. 8, three experimental conditions are shown, namely horizontal lidar measurements at an altitude of 1, 10, and 100 m. In these calculations, it is assumed that the atmospheric parameter C_n^2 is uniform along the horizontal lidar propagation path, with a value of $C_n^2 = 1 \times 10^{-12}$, 5×10^{-14} , and $2 \times 10^{-15} \text{ m}^{-2/3}$ at $h = 1, 10, \text{ and } 100 \text{ m}$, respectively. As seen in Fig. 8, the maximum effective receiver telescope diameter for a ground-based heterodyne Nd:YAG lidar at 1.06 μ m may be quite small, depending on the level of atmospheric turbulence. These results also imply that a heterodyne Nd:YAG lidar has higher efficiency for airborne measurements. For ground-based operation, it will suffer from greater receiver coherence loss because of the smaller atmospheric speckle size. In the latter case, however, one may use a 2-D detector array to perform heterodyne speckle averaging which will enhance the detection CNR and help to overcome this limitation.³¹ [Note added in Proof: We have also recently used a Monte Carlo simulation method³¹ to predict the reduced heterodyne detection efficiency due to atmospheric turbulence, and have found similar results as those shown in Fig. 6.]

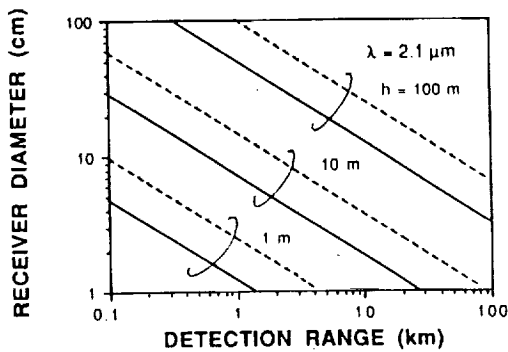


Fig. 9. Calculated results of the maximum effective receiver telescope diameter (solid lines) and the practically useful telescope diameter (dashed lines) for a 2.1- μm Ho heterodyne lidar as a function of detection range. The atmospheric parameters are the same as those used in Fig. 8.

C. Predictions for Coherent Doppler 2- μm Ho Lidar

We have used the above theory (Sec. II) to predict the performance of a coherent Doppler 2.1- μm Ho lidar. Such a Ho lidar is particularly useful for remote sensing because of its eye-safe wavelength and potential for diode laser pumping. Figure 9 shows the calculated result of $d_r = 3\rho_0$ (solid lines) and $d_r = 6\rho_0$ (dashed lines) for a heterodyne Ho lidar operated in the same experimental and atmospheric conditions as those of Fig. 8. By comparing the results in Figs. 8 and 9, it can be seen that a larger receiver telescope aperture can be effectively employed for heterodyne lidar detection at the longer wavelength, since ρ_0 at $\lambda = 2.1 \mu\text{m}$ is estimated to be ~ 2.3 times larger than that at $\lambda = 1.06 \mu\text{m}$. For the ground-based heterodyne Ho lidar measurement at a range of $R = 1\text{--}2 \text{ km}$, the maximum effective telescope diameter $d_{\text{eff,max}} = 3\rho_0$ could be larger than 5 cm. At the higher altitude of $h = 100 \text{ m}$, $d_{\text{eff,max}} \cong 40 \text{ cm}$ at $R = 1 \text{ km}$, and $d_{\text{eff,max}} \cong 10 \text{ cm}$ at $R = 10 \text{ km}$. These predictions indicate that the operating performance of a coherent Doppler Ho lidar will only be marginally reduced by atmospheric turbulence. Of course, further experiments will have to be conducted to verify these predictions.

D. Comparison of Heterodyne and Direct Detection CNR at 1 and 10 μm

In our experiments with the short pulse, coherent Nd:YAG lidar at 1.06 μm , we found that nearly equal CNRs were measured with heterodyne and direct detection of lidar radiation backscattered from atmospheric aerosols at a relatively short range of $\sim 500 \text{ m}$. To compare this experimental observation to the theory, we examine the ratio of heterodyne CNR to direct detection CNR, $\Gamma = \text{CNR}_{H,\text{av}}/\text{CNR}_D$, which, from Eqs. (3), (6), and (9), is given by

$$\Gamma = (\eta/h\nu B) F_0(\rho_0, d_r) G (\text{NEP}_{\text{th}}^2 + \text{NEP}_{\text{at}}^2)^{1/2}, \quad (12)$$

where we have added CNR reduction factor G for heterodyne detection, which, as mentioned earlier, is to compensate for the signal loss from mismatch in optical alignment. Figure 10(a) shows the calculated result of Γ for a ground-based ($h = 10 \text{ m}$, horizontal

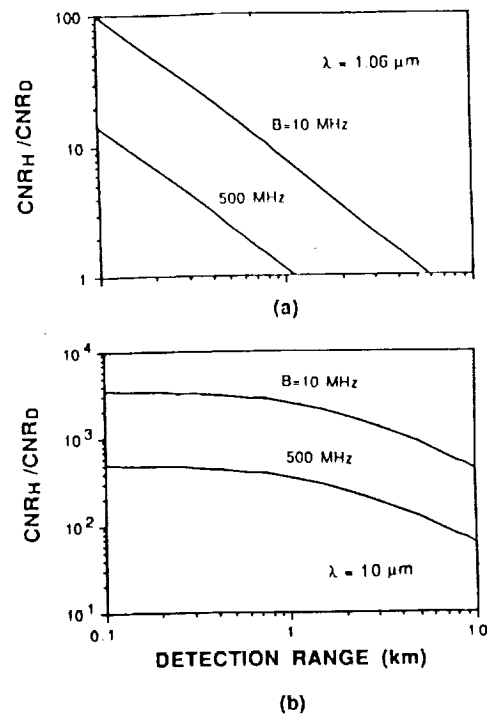


Fig. 10. Comparison of heterodyne and direct detection CNR for a ground-based (a) 1- μm Nd:YAG lidar and (b) 10- μm CO₂ lidar, both using a 20-cm diam receiver telescope. The atmospheric parameter $C_n^2 = 5 \times 10^{-14} \text{ m}^{-2/3}$ is assumed to be uniform along the lidar propagation path and two different electrical bandwidths of 10 and 500 MHz are shown.

propagation path) Nd:YAG lidar, where two electrical detection bandwidths were taken as parameters, namely, $B = 500 \text{ MHz}$ for high velocity (1-km/s) Doppler measurement, and $B = 10 \text{ MHz}$ for conventional wind sensing. The other typical values were $\lambda = 1.06 \mu\text{m}$, $C_n^2 = 5 \times 10^{-14} \text{ m}^{-2/3}$, $\eta = 0.8$, $I_D = 2 \text{ nA}$, $I_E = 3 \mu\text{A}$, $d_r = 20 \text{ cm}$, and $G = 0.4$. As seen in Fig. 10(a), for $B = 500 \text{ MHz}$, $\Gamma \cong 3$ at $R = 500 \text{ m}$, showing good agreement with our experimental result. This also indicates that while a wide bandwidth heterodyne lidar at 1 μm is feasible for high velocity Doppler measurement, it does not provide a much higher detection sensitivity compared with that of a direct detection lidar. However, as seen in Fig. 10(a), for a conventional Doppler wind sensing application where B is $\sim 10 \text{ MHz}$, the heterodyne detection technique still offers the advantage of higher sensitivity at a detection range up to several kilometers.

The result of Fig. 10(a) appears to differ from previous experiments of heterodyne detection using 10- μm CO₂ laser sources, where the heterodyne detection CNR can be several orders of magnitude greater than that of direct detection,²⁴ and range-resolved atmospheric aerosol lidar measurements using CO₂ heterodyne lidars have been made at ranges up to 20 km.^{32,33} This is due to the fact that at a 10- μm wavelength, the photon energy is $\sim 1/10$ smaller and the value of ρ_0 is approximately sixteen times larger compared with those at 1 μm . To illustrate this, Fig. 10(b) shows the calculated result of Γ for a ground-based CO₂ lidar at

10 μm . It is assumed in this example that a liquid nitrogen cooled HgCdTe detector is used, with $\text{NEP}_{DL} = 10^{-12} \text{ W/Hz}^{1/2}$. The other system and experimental values are the same as those used for the Nd:YAG lidar. It is clearly shown in Fig. 10(b) that the heterodyne detection technique at the 10- μm wavelength offers superior detection sensitivity compared with that of the direct detection. The detection sensitivity of a CO_2 heterodyne lidar will be only marginally reduced by atmospheric refractive turbulence when the detection range is up to 1–2 km. However, for long-range remote sensing applications, it is still necessary to consider the effects of atmospheric turbulence on the effective receiver aperture of a CO_2 heterodyne lidar.

V. Conclusions

In this paper, we have presented an experimental study of heterodyne and direct detection of lidar propagation through the turbulent atmosphere. It has been observed that for heterodyne lidar detection at 1 μm , serious receiver coherence loss occurred as the result of atmosphere turbulence. At a relatively short detection range of 450 m, the maximum effective receiver telescope diameter was as small as 4 cm. The effective receiver telescope diameter was also observed to vary during the day as the atmospheric conditions and the turbulence level changed. On the other hand, as expected, atmospheric turbulence did not affect the direct detection CNR. Likewise, because of the small atmospheric speckle size at 1 μm , the statistical fluctuation in the direct detection lidar signal returns was significantly reduced by aperture speckle averaging. Of course, more extensive experimental studies that involve heterodyne lidar measurement at various altitudes/ranges and direct measurements of C_n^2 are required to better understand these effects.

Our observed limitation on the effective receiver size for 1- μm heterodyne lidar agrees in functional form with the related predictions on atmospheric turbulence and heterodyne detection as given by Fried¹² and Clifford and Wanzura.¹⁹ Based on our experimental work and these previous theories, we have also made an analytical study of the predicted performance of different lidar systems operated in various experimental and atmospheric conditions. It was found that a coherent 1- μm Nd:YAG lidar may be severely impacted by atmospheric turbulence for ground-based measurements and less so for upper altitude studies. The predictions for a coherent 2- μm Ho lidar indicate that some reduction is expected in highly turbulent conditions or when receiver telescopes with very large aperture size are used. In such cases, some enhancement in the heterodyne Doppler measurement performance could be gained through the use of a 2-D heterodyne detector array to perform speckle averaging at the detector plane.

Finally, it is our hope that our experimental lidar data will encourage the development of the appropriate atmospheric turbulence and heterodyne lidar detection theory which is directly applicable to a general

class of lidar systems, so that a more precise comparison of lidar data can be made.

This work was supported in part by the Office of Naval Research, the Florida High Technology and Industrial Council, and NASA/Langley Research Center.

References

1. See, for example, Special Issue on Solid-State Lasers, IEEE J. Quantum Electron. **QE-24** (June 1988). For latest reports, see papers in *Technical Digest, Topical Meeting on Advanced Solid-State Lasers* (Optical Society of America, Washington, DC, 1990).
2. N. Menyuk and D. K. Killinger, "Atmospheric Remote Sensing of Water Vapor, HCl, and CH_4 Using a Continuously Tunable Co:MgF_2 Laser," *Appl. Opt.* **26**, 3061–3065 (1987).
3. T. J. Kane, W. J. Kozlovsky, R. L. Byer, and C. Byvik, "Coherent Laser Radar at 1.06 μm Using Nd:YAG Lasers," *Opt. Lett.* **12**, 239–241 (1987).
4. M. J. Kavaya, S. M. Henderson, J. R. Magee, C. P. Hale, and R. M. Huffaker, "Remote Wind Profiling with a Solid-State Nd:YAG Coherent Lidar System," *Opt. Lett.* **14**, 776–778 (1989).
5. N. Sugimoto, N. Sims, K. Chan, and D. K. Killinger, "Eye-Safe 2.1- μm Ho Lidar for Measuring Atmospheric Density Profiles," *Opt. Lett.* **15**, 302–304 (1990).
6. K. P. Chan and D. K. Killinger, "Short-Pulse, Coherent Doppler Nd:YAG Lidar," *Opt. Eng.* **30**, 49–54 (1991).
7. R. T. Menzies and R. M. Hardesty, "Coherent Doppler Lidar for Measurements of Wind Field," *Proc. IEEE* **77**, 449–462 (1989).
8. V. I. Tatarski, "The Effects of the Turbulent Atmosphere on Wave Propagation," in *IPST Catalog 5319* (National Technical Information Service, Springfield, VA 22151, 1971).
9. J. W. Strohbehn, Ed., *Laser Beam Propagation in the Atmosphere* (Springer-Verlag, New York, 1978), and references therein.
10. V. A. Banakh and V. L. Mironov, *Lidar in a Turbulent Atmosphere* (Artech House, Boston, 1987).
11. I. Goldstein, P. A. Miles, and A. Chabot, "Heterodyne Measurement of Light Propagation Through Atmospheric Turbulence," *Proc. IEEE* **53**, 1172–1180 (1965).
12. D. L. Fried, "Optical Heterodyne Detection of an Atmospherically Distorted Signal Wave Front," *Proc. IEEE* **55**, 57–67 (1967).
13. J. H. Churnside and C. M. McIntyre, "Signal Current Probability Distribution for Heterodyne Receiver in the Turbulent Atmosphere. 1: Theory," *Appl. Opt.* **17**, 2141–2147 (1978).
14. J. H. Churnside and C. M. McIntyre, "Signal Current Probability Distribution for Heterodyne Receiver in the Turbulent Atmosphere. 2: Experiment," *Appl. Opt.* **17**, 2148–2152 (1978).
15. P. A. Pincus, M. E. Fossey, J. Holmes, and J. R. Kerr, "Speckle Propagation Through Turbulence: Experimental," *J. Opt. Soc. Am.* **68**, 760–762 (1978).
16. H. T. Yura, "Signal-to-Noise Ratio of Heterodyne Lidar Systems in the Presence of Atmospheric Turbulence," *Opt. Acta* **26**, 627–644 (1979).
17. R. L. Schwiesow and R. F. Calfee, "Atmosphere Refractive Effects on Coherent Lidar Performance at 10.6 μm ," *Appl. Opt.* **18**, 3911–3917 (1979).
18. J. F. Holmes, M. H. Lee, and J. R. Kerr, "Effect of the Log-Amplitude Covariance Function on the Statistics of Speckle Propagation through the Turbulent Atmosphere," *J. Opt. Soc. Am.* **70**, 355–360 (1980).

19. S. F. Clifford and S. Wandzura, "Monostatic Heterodyne Lidar Performance: The Effect of the Turbulent Atmosphere," *Appl. Opt.* **20**, 514-516 (1981); "Monostatic Heterodyne Lidar Performance: The Effect of the Turbulent Atmosphere, Correction," *Appl. Opt.* **20**, 1502 (1981).
20. J. H. Shapiro, B. A. Capron, and R. C. Harney, "Imaging and Target Detection with a Heterodyne-Reception Optical Radar," *Appl. Opt.* **20**, 3292-3313 (1981).
21. B. J. Rye, "Refractive-Turbulence Contribution to Incoherent Backscatter Heterodyne Lidar Returns," *J. Opt. Soc. Am.* **71**, 687-691 (1981).
22. R. Murty, "Refractive Turbulence Effects on Truncated Gaussian Beam Heterodyne Lidar," *Appl. Opt.* **23**, 2498-2502 (1984).
23. Y. Zhao, M. J. Post, and R. M. Hardesty, "Receiving Efficiency of Monostatic Pulsed Coherent Lidars. 1: Theory," *Appl. Opt.* **29**, 4111-4119 (1980).
24. R. H. Kingston, *Detection of Optical and Infrared Radiation* (Springer-Verlag, New York, 1978).
25. J. W. Goodman, "Statistical Properties of Laser Speckle Patterns," in *Laser Speckle and Related Phenomena*, J. C. Dainty, Ed. (Springer-Verlag, New York, 1975), Chap. 2, pp. 9-75.
26. N. Sugimoto, K. P. Chan, and D. K. Killinger, "Video Camera Measurement of Atmospheric Turbulence Using the Telescope Image of a Distant Light Source," *Appl. Opt.* **30**, 365-367 (1991).
27. J. C. Wyngard, Y. Izumi, and S. A. Collins, Jr., "Behavior of the Refractive-Index-Structure Near the Ground," *J. Opt. Soc. Am.* **61**, 1646-1650 (1971).
28. D. K. Killinger, N. Menyuk, and W. E. DeFeo, "Experimental Comparison of Heterodyne and Direct Detection for Pulsed Differential Absorption CO₂ Lidar," *Appl. Opt.* **22**, 682-689 (1983).
29. S. C. Cohen, "Heterodyne Detection: Phase Front Alignment, Beam Spot Size, and Detector Uniformity," *Appl. Opt.* **14**, 1953-1959 (1975).
30. J. Y. Wang, "Detection Efficiency of Coherent Optical Radar," *Appl. Opt.* **23**, 3421-3427 (1984).
31. N. Sugimoto, K. P. Chan, and D. K. Killinger, "Optimal Heterodyne Detection Array Size for 1- μ m Coherent Lidar Propagation through Atmospheric Turbulence," *Appl. Opt.* **30**, this issue (1991).
32. R. T. Menzies, M. J. Kavaya, P. H. Flamant, and D. A. Haner, "Atmospheric Aerosol Backscatter Measurements Using a Tunable Coherent CO₂ Lidar," *Appl. Opt.* **23**, 2510-2517 (1984).
33. R. M. Hardesty, "Coherent DIAL Measurement of Range-Resolved Water Vapor Concentration," *Appl. Opt.* **23**, 2545-2553 (1984).

Coherent 1- μm lidar measurements of atmospheric-turbulence-induced spatial decorrelation using a multi-element heterodyne detector array

Kin Pui Chan and Dennis K. Killinger

We have employed a coherent 1- μm Nd:YAG lidar system to measure directly, for the first time to our knowledge, the reduced spatial coherence length, ρ_0 , of the lidar returns caused by atmospheric turbulence. Our experiments were conducted by using a 2×2 heterodyne detector array, which permitted real-time spatial correlation measurements of the lidar returns at two different detector spacings. The spatial correlation coefficients and spatial coherence length of the lidar returns from a hard target were measured during a day-to-night time period when the atmospheric turbulence parameter, C_n^2 , was measured to vary from 2×10^{-13} to $2 \times 10^{-14} \text{ m}^{-2/3}$. These directly measured values of ρ_0 as a function of C_n^2 were found to be in good agreement with theoretical predictions.

I. Introduction

To date, the majority of coherent Doppler lidars have used CO_2 laser sources at $10 \mu\text{m}$.¹ In recent years, however, there has been an increased interest in the development of coherent Doppler lidars that employ newly emerging solid-state laser technology; several coherent Doppler lidars using 1–2- μm solid-state lasers have been developed by different groups.^{2–5} Recently we experimentally measured the effect of atmospheric turbulence on a coherent 1- μm lidar system and found that the receiver coherence loss caused by atmospheric turbulence was much more severe at 1–2 μm than at $10 \mu\text{m}$.⁶ Such receiver coherence loss has been related to the atmospheric-turbulence field coherence length, ρ_0 , in several optical propagation-detection theories.^{7–10} Although the characteristics of ρ_0 are fairly well understood,¹¹ there have been few coherent lidar measurements that have measured the value of ρ_0 directly. Such experimental information is particularly important for the development of these shorter wavelength solid-state coherent lidars.

In this paper, we report, for the first time to our knowledge, the direct, real-time measurement of the

spatial correlation of the heterodyne (coherent) lidar signals under different conditions of moderate-to-strong atmospheric turbulence. Our lidar measurements were conducted by using a short-pulse (8-ns) coherent Nd:YAG bistatic lidar system and a 2×2 heterodyne detector array, which provided four independent heterodyne lidar signal outputs. The statistical cross correlation of the independent signals was obtained for the two different detector pair spacings and directly yielded the value of ρ_0 . This direct measurement of ρ_0 was also compared with the value of ρ_0 that was determined from our measurements of the atmospheric turbulence parameter C_n^2 . Good agreement was observed in these measurements.

Our spatial correlation measurements are unique in that a coherent lidar has been used, but they are similar in functional form to previous lidar or laser propagation experiments that used point-source direct-detection detectors. For example, Pincus *et al.* measured the spatial covariance function of laser speckle propagating through the turbulent atmosphere, using a visible Ar^+ -ion laser and two spatially separated direct-detection detectors.¹² More recently, Churnside *et al.* measured the strong optical scintillation in the atmosphere, using an Ar^+ laser and a one-dimensional direct-detection detector array.¹³ What is valuable about the experiments presented in this paper is that it is what we believe is the first 1- μm heterodyne lidar experiment that directly measures the value of ρ_0 under different atmospheric turbu-

The authors are with the Department of Physics, University of South Florida, Tampa, Florida 33620.

Received 30 April 1991.

0003-6935/92/000001-06\$05.00/0.

© 1992 Optical Society of America.

lence levels. The values of ρ_0 were found to be consistent with our earlier measurements of the effective receiver telescope aperture size for a 1- μm coherent Nd:YAG lidar.^{6,14}

II. Analytical Background

When lidar radiation is transmitted onto a diffuse target, the resultant backscattered speckle lobe will be randomly perturbed by atmospheric turbulence as it propagates backward to the transmitter-receiver. Although this target speckle-atmospheric turbulence interaction is a complex subject, an approximate analysis of the relative size of the target speckle and the influence of atmospheric turbulence can be made as follows. As a first-order approximation, the diameter of the target speckle, d_s , may be calculated by¹⁵

$$d_s = 2\lambda R/D, \quad (1)$$

where λ is the laser wavelength, R is the transmitter-receiver to target range, and D is the diameter of the transmitted laser beam on the target. As Eq. (1) shows, d_s is larger at longer distances. In other words, the target speckle size becomes larger for longer-range coherent lidar measurements in the absence of atmospheric turbulence. As a numerical example, for a Nd:YAG laser wavelength of $\lambda = 1.06 \mu\text{m}$ and $D = 10 \text{ cm}$, it is calculated that $d_s \cong 2$ and 20 cm at $R = 1$ and 10 km , respectively.

One of the atmospheric turbulence effects on lidar propagation is the reduction of the spatial coherence length of the lidar beam. In particular, the atmospheric turbulence field coherence length ρ_0 may be calculated by^{10,11}

$$\rho_0 = \left[2.91 k^2 \int_0^R C_n^2(z)(1-z/R)^{5/3} dz \right]^{3/5}, \quad (2)$$

where k is the wave number and C_n^2 is the refractive-index structure parameter of the atmosphere. For the case in which C_n^2 is assumed to be uniformly distributed along the propagation path, such as in a horizontal path, Eq. (2) becomes

$$\rho_0 = (1.09 k^2 R C_n^2)^{-3/5}. \quad (3)$$

Equation (3) is often used to deduce the value of ρ_0 from the experimentally measured value of C_n^2 ; the value of C_n^2 is measured most often by using a scintillometer. Equations (2) and (3) are valid for lidar propagation where the signal transverse coherence length is larger than the inner scale of the turbulence cells, which causes coherence loss. As Eq. (3) shows, ρ_0 is inversely proportional to the detection range. In other words, the spatial transverse dimensions over which the received lidar signal is spatially coherent becomes smaller as the detection range is increased, so the atmospheric turbulence effect is also enhanced. For $\lambda = 1.06 \mu\text{m}$ and a typical value of $C_n^2 = 5 \times 10^{-14} \text{ m}^{-2/3}$ measured near the ground, ρ_0 is calculated to be ~ 1 and 0.25 cm at $R = 1$ and 10 km ,

respectively. By comparison of the above-calculated results of d_s and ρ_0 , it is seen that for long-range 1- μm coherent lidar measurements the strong path-integrated atmospheric turbulence may be the dominant source in the reduction of the spatial coherence length of the lidar returns.

The technique used in this paper is to obtain the value of ρ_0 directly from the relative spatial cross-correlation coefficients of lidar signals that are measured with a multielement detector array. Such a correlation measurement technique has been used by Pincus *et al.*¹² who have also theoretically analyzed the first- and second-order statistics of laser target speckle that is perturbed by atmospheric turbulence.^{16,17} Although their generalized equations covering weak-to-strong path-integrated atmospheric turbulence are quite complex, their work also indicates that for weak-to-moderate atmospheric turbulence corresponding to Rytov variance, $\sigma_r^2 = 0.124 C_n^2 k^{-7/6} R^{11/6}$, of less than approximately 0.02, the cross-correlation coefficient function of the two lidar signals, $C_c(r)$, can be approximated for the simple case of a focused transmitted beam as¹⁶

$$\begin{aligned} C_c(r) &= (I_2(\mathbf{r}_2) - \langle I_1 \rangle) (I_1(\mathbf{r}_1) - \langle I_1 \rangle) / \sigma_r \sigma_r \\ &= \exp \left[-2 \left(\frac{r}{D_t} \right)^2 - 5.82 k^2 \right. \\ &\quad \left. \times \int_0^R C_n^2(z) (1-z/R)^{5/3} r^{5/3} dz \right], \end{aligned} \quad (4)$$

where $I_1(\mathbf{r}_1)$ and $I_2(\mathbf{r}_2)$ are the signal intensities that are received by the two point detectors that are separately located on the receiver aperture plane, $r = |\mathbf{r}_2 - \mathbf{r}_1|$ is the detector spacing, and D_t is the diameter of the laser beam on the transmitter aperture plane. From Eqs. (2) and (4) we have

$$C_c(r) = \exp[-2(r/D_t)^2 - 2(r/\rho_0)^{5/3}]. \quad (5)$$

The term of $2(r/\rho_0)^{5/3}$ in Eq. (5) differs from that of $4(r/\rho_0)^{5/3}$ in Eq. (47) of Ref. 16 by a factor of 2. This difference is, however, merely due to different numerical definitions of ρ_0 that were derived from the definitions of the wave structure function, $D_w = (r/\rho_0)^{5/3}$, used in Refs. 10 and 11, and $D_w = 2(r/\rho_0)^{5/3}$, used in Ref. 16, respectively. The value of ρ_0 given by Eq. (2) is thus larger than that in Ref. 16 by a factor of $2^{3/5}$, i.e., ~ 1.5 . Consequently, Eq. (5) agrees with Eq. (47) in Ref. 16. In this study, the value of ρ_0 was calculated by using Eq. (2) so that the result would be consistent with our previous reports.^{6,14}

As can be seen from Eq. (5), if D_t is a constant the value of ρ_0 can be deduced from the measured values of C_c at different detector spacings. In Section III, examples of real-time direct measurements of ρ_0 made with a 2×2 heterodyne detector array are given, followed by an analysis of the spatial correlation coefficients under different atmospheric turbulence levels.

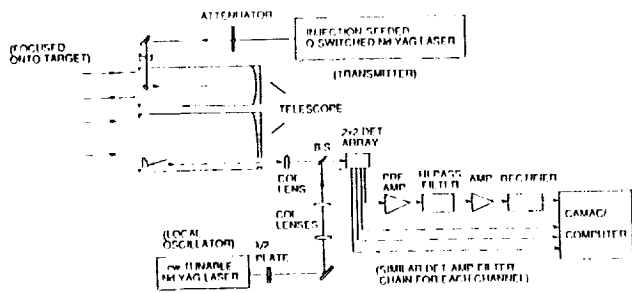


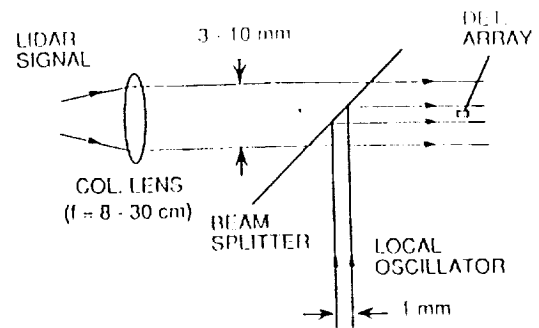
Fig. 1. Schematic of 1- μ m coherent Nd:YAG lidar system employing a 2×2 heterodyne detector array. B.S., beam splitter.

III. Experiment

Experimental Setup

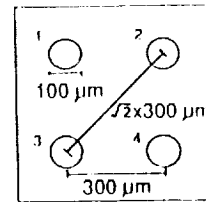
A schematic of our experimental setup is shown in Fig. 1. Our lidar experiments were conducted by employing a short-pulse (8-ns) coherent Nd:YAG lidar⁴ and a 2×2 heterodyne detector array. After being attenuated to a pulse energy of ~ 5 mJ, the output of the injection-seeded, single-frequency, flash-lamp-pumped, Q-switched Nd:YAG laser was fully expanded and transmitted by a 13-cm-diameter Newtonian telescope to a hard target (brick wall) at a distance of ~ 450 m. The transmitted laser beam was focused onto the target, whose focused beam diameter was ~ 1 cm. The lidar return signals were collected by an 18-cm-diameter off-axis parabolic telescope with a 5-m long effective focal length. The transmitter and receiver telescopes were placed in a bistatic configuration with a 25-cm separation between optic axes. The lidar propagation path was nearly horizontal at a height of ~ 6 m above the ground.

Figure 2(a) is a schematic of our heterodyne receiver-detector. The lidar signal was collected with the receiver telescope and collimated by using a lens whose focal length was changed to vary the projected detector spacings on the telescope aperture plane. The collimated signal beam was then combined with the collimated, 1-mm-diameter local-oscillator beam by using a 50/50 beam splitter and was not focused onto the 2×2 detector array. Therefore both the lidar signal and the local-oscillator beam were projected as a plane-wave (i.e., collimated) beam onto the detector surface. Figure 2(b) illustrates the geometrical dimensions of the detector array, on which four identical 100- μ m-diameter, 1-GHz-band-width InGaAs photodiode detectors (Epitaxx ETX100) were integrated with a 300- μ m center-to-center separation; the spatial separation of the two diagonal elements was $2 \times 300 \mu\text{m}$. As Fig. 2 shows, the projected detector spacing on the receiver telescope aperture plane, r , may be calculated by using the geometrical optics equation $r = r_d f_r / f_c$, where r_d is the detector spacing on the detector array surface and f_r and f_c are the focal length of the receiver telescope and the collimating lens, respectively. By choosing $f_c = 8$ –30 cm in a series of lidar measurements where $f_r = 5$ m



(a)

2x2 InGaAs DETECTOR ARRAY



(b)

Fig. 2. (a) Schematic of the coherent receiver-detector designed for the spatial cross-correlation measurement and (b) geometric dimensions of the 2×2 detector array.

and $r_d = 300 \mu\text{m}$, we were able to vary r over the range of 0.5–1.9 cm.

The heterodyne signal intermediate frequency was set at ~ 500 MHz by frequency tuning the laser-diode-pumped, cw 4-mW Nd:YAG local oscillator. The heterodyne signal outputs from the four array elements were simultaneously acquired in real time by using a four-channel signal-acquisition system, in which each channel consisted of a 23 dB preamplifier (Analog Modules 710-47), a high-pass filter (Mini-Circuit SHP-300), a 26-dB amplifier (Mini-Circuit ZFL-500), and a microwave detector that was used as a rectifier (Narda 4503). The four-channel signals were transferred to a computer-controlled CAMAC system, which included a 12-channel variable-gain amplifier (Phillips Scientific 7177) and a high-speed 12-channel analog-to-digital converter (Lecroy 2249W). Because no square-law detector was used, the digitized heterodyne lidar signal was squared before data processing in the computer to be comparable with that of standard heterodyne detection theory.¹⁸ The lidar system was operated at a 10-Hz repetition rate.

Results

Heterodyne lidar measurements were conducted under a variety of atmospheric conditions. Figure 3 shows typical results of the heterodyne lidar signal intensity that was measured from each of the four detector elements of the 2×2 array as a function of time and that was taken during nighttime. Six hun-

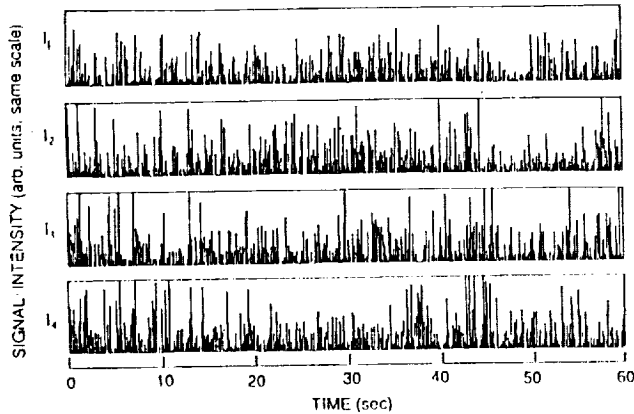


Fig. 3. Intensity of heterodyne lidar returns from a hard target as a function of time, detected by the individual detector elements of the 2×2 detector array.

dred lidar return pulses were measured over a time period of 60 s. In this measurement, the focal length of the collimating lens was chosen as 7.8 cm, so the projected detector spacing on the receiver telescope aperture plane was estimated to be ~ 1.9 cm and ~ 2.7 cm for the 300- and 2×300 - μm separated detectors, respectively. As Fig. 3 shows, the four individual signal outputs from the 2×2 detector array, I_1 - I_4 , are partially correlated, showing some evidence of signal wave-front distortion caused by atmospheric turbulence. The average intensities of the four channel signals were found to be nearly equal, and the statistics of the signals also followed a Rayleigh distribution with nearly unity signal standard deviation.¹⁶ During this nighttime experiment, the atmospheric turbulence parameter C_n^2 was measured as $C_n^2 = 1.5 \times 10^{-14} \text{ m}^{-2/3}$ by a C_n^2 long-path scintillometer.

From the four-channel signals shown in Fig. 3, the cross-correlation coefficient C_i was measured to be 0.49 and 0.28 for the projected detector spacing of 1.9 and 2.7 cm, respectively. These two relative C_i values can be used in Eq. (5) to obtain a value of ρ_0 . Substituting the experimental data of $C_i \approx 0.49$ for $r \approx 1.9$ cm and $C_i' \approx 0.28$ for $r \approx 2.7$ cm into Eq. (5) yields a value of $\rho_0 \approx 3.6$ cm.

This experimental value of ρ_0 can be compared with that obtained by using Eq. (3), which relates ρ_0 to C_n^2 . When the measured values of $C_n^2 = 1.5 \times 10^{-14} \text{ m}^{-2/3}$ and $R = 450$ m are used, Eq. (3) predicts a value of $\rho_0 = 3.6$ cm, which is in excellent agreement with that measured above with the correlation measurement technique that used a 2×2 detector array.

We have also measured the spatial correlation values of lidar returns that are associated with different atmospheric turbulence levels. Fig. 4 shows the measured lidar signal cross-correlation coefficient as a function of the projected detector spacing on the receiver telescope aperture plane; the projected detector spacing was varied by changing the focal length of the collimating lens. Lidar experimental data were obtained under two atmospheric-turbulence levels, corresponding to $C_n^2 = 2 \times 10^{-14} \text{ m}^{-2/3}$ and $2 \times 10^{-13} \text{ m}^{-2/3}$

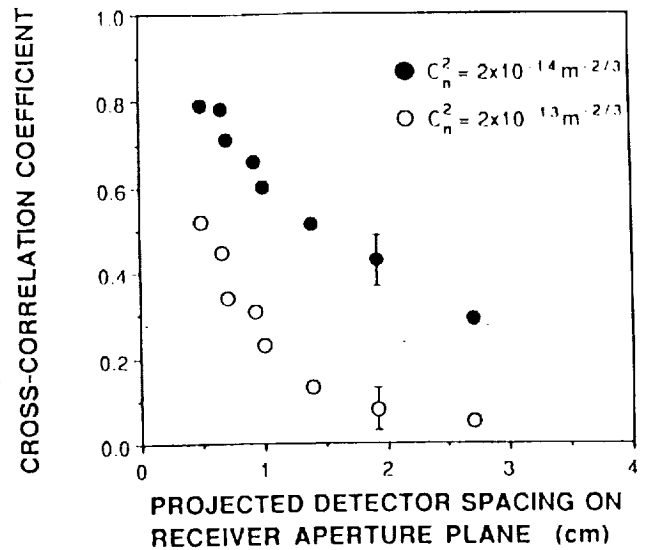


Fig. 4. Measured cross-correlation coefficients as functions of the projected detector spacing on the receiver telescope aperture plane under two different atmospheric-turbulence levels.

$\text{m}^{-2/3}$, and over a 2-h period when the value of C_n^2 varied by less than $\pm 10\%$. As Fig. 4 shows, the cross-correlation coefficient C_i is, as expected from Eqs. (4) and (5), much smaller at the higher turbulence level. For $C_n^2 = 2 \times 10^{-14} \text{ m}^{-2/3}$, i.e., for a typical night-time lidar experiment, the value of C_i could be reduced by atmospheric turbulence to $\exp(-1)$ for a relatively small detector separation of ~ 3 cm. For the daytime measurement where $C_n^2 = 2 \times 10^{-13} \text{ m}^{-2/3}$, however, a similar value of C_i was measured for a much smaller detector separation of nearly 1 cm.

Figure 5 shows a direct comparison of our experimental result with the analytical predictions for the moderate atmospheric turbulence levels corresponding to $C_n^2 \approx 10^{-14} \text{ m}^{-2/3}$. The measured cross-correlation coefficients (filled circles) are repeated

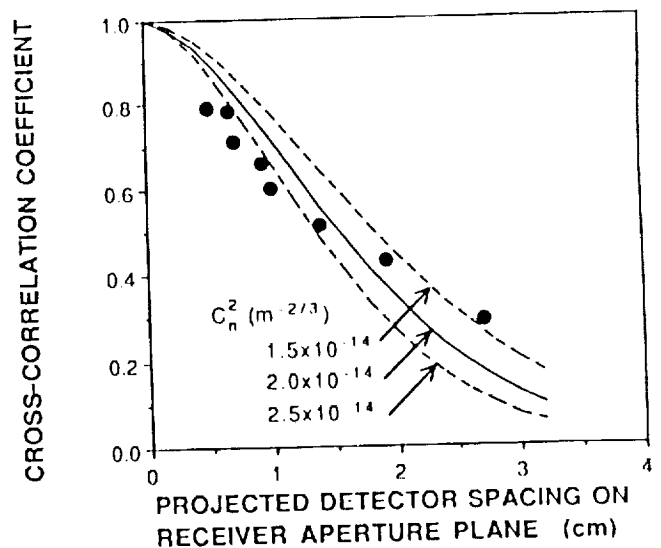


Fig. 5. Comparison of measured cross-correlation coefficients (filled circles) and the analytical predictions (solid and dashed lines) made by using Eqs. (3) and (4) for different close values of C_n^2 .

from Fig. 4), and the analytical predictions (solid and dashed lines) were obtained by using Eqs. (3) and (5) to calculate ρ_0 and $C_r(r)$, respectively; $C_n^2 = 1.5 \times 10^{-14}$, 2.0×10^{-14} , and $2.5 \times 10^{-14} \text{ m}^{-2/3}$ were used. As Fig. 5 shows, our experimental data are in fairly close agreement with the analytical predictions.

It is also found from Fig. 5 that the measured results deviate somewhat from the analytical predictions in such a manner that the measured values of C_r were slightly smaller than that predicted for the detector spacing of less than $\sim 1.5 \text{ cm}$ ($\sim \rho_0/2$) and were greater than that predicted for the larger spacing. This deviation may be due to the finite size (nonpoint source) of the $100\text{-}\mu\text{m}$ -diameter detector elements that were projected onto the receiver plane. In our measurements, where $f_r = 500 \text{ cm}$ and $f_c = 8\text{--}30 \text{ cm}$, the projected finite size of the detector was calculated to be in the range of $0.2\text{--}0.8 \text{ cm}$, which is a possible contribution to the deviation observed. Another source of measurement error that may contribute to this deviation is the variation of C_n^2 value during the measurement. As can be seen from Fig. 5, the functional form of the cross-correlation coefficient is determined uniquely by the C_n^2 value. Consequently, a possible $\pm 10\%$ variation in C_n^2 value during our measurements, which typically took $\sim 2 \text{ h}$ to complete, may affect the functional form of the measured results to a certain extent. Meanwhile, the possible variation in C_n^2 value along the horizontal lidar propagation path may also contribute to this deviation.

Finally, the experimental data shown in Fig. 4 (open circles) for the stronger atmospheric turbulence level of $C_n^2 = 2 \times 10^{-13} \text{ m}^{-2/3}$ were also compared with the theoretical prediction of Eq. (4) but showed significant deviation. This deviation was not surprising, because Eq. (4) is not valid for the strong-turbulence case where the Rytov variance σ_r^2 is much greater than 0.02 .¹⁷ For the experimental data shown in Fig. 4 (open circles), σ_r^2 was calculated from C_n^2 value to be ~ 0.14 . Moreover, because the measured coherence length of $\sim 1 \text{ cm}$ was less than the Fresnel-zone size $(R\lambda)^{1/2} \cong 2 \text{ cm}$, the measured result may be partially due to intensity fluctuation (scintillation) that is not characterized by Eq. (4). Equation (4), obtained from Ref. 16, was originally derived to include for simplicity only terms involving the phase and not the log-amplitude term in the wave-structure function. Thus Eq. (4) does not consider the effects associated with the Fresnel zone size, $(R\lambda)^{1/2}$. However, these experimental data were found to be similar in functional form to the theoretical prediction in Fig. 2 of the paper by Holmes *et al.*,¹⁷ which is valid for the strong atmospheric-turbulence levels.

IV. Summary

We have conducted coherent $1\text{-}\mu\text{m}$ lidar measurements of atmospheric-turbulence-induced spatial decorrelation under the conditions of moderate-to-strong atmospheric turbulence. Our measurement method, which employed a 2×2 heterodyne detector

array, was demonstrated to be useful for a simple, direct measurement of ρ_0 . The spatial cross-correlation coefficient of the lidar returns from a hard target at a range of 450 m was measured to be reduced by atmospheric turbulence to a value of $\exp(-1)$ at a relatively small projected detector spacing of approximately 1 and 3 cm for typical daytime and nighttime measurements, respectively. The measured results of ρ_0 were found to be in excellent agreement with the ρ_0 value that was deduced from the measurement of C_n^2 by a long-path scintillometer.

Our original intent in using the heterodyne detector array was to improve the signal-to-noise ratio of the coherent $1\text{-}\mu\text{m}$ lidar system through coherent addition of the atmospheric-turbulence-distorted lidar returns.¹⁴ As we have shown in this paper, an added benefit of such a detector array is its ability to measure directly the value of ρ_0 .

This research was supported in part by the U.S. Office of Naval Research, by a SBIR grant through Schwartz Electro-Optics, and by NASA/Langley Research Center. We thank J. H. Churnside and R. M. Hardesty of the NOAA/Wave Propagation Laboratory for the loan of the C_n^2 scintillometer instrument. Also, we thank the reviewers for their useful suggestions.

References

1. R. T. Menzies and R. M. Hardesty, "Coherent Doppler lidar for measurements of wind field," *Proc. IEEE* **77**, 449-462 (1989).
2. T. J. Kane, W. J. Kozlovsky, R. L. Byer, and C. Byvik, "Coherent laser radar at $1.06 \mu\text{m}$ using Nd:YAG lasers," *Opt. Lett.* **12**, 239-241 (1987).
3. M. J. Kavaya, S. M. Henderson, J. R. Magee, C. P. Hale, and R. M. Huffaker, "Remote wind profiling with a solid-state Nd:YAG coherent lidar system," *Opt. Lett.* **14**, 776-778 (1989).
4. K. P. Chan and D. K. Killinger, "Short pulse coherent doppler Nd:YAG lidar," *Opt. Eng.* **30**, 49-54 (1991).
5. S. M. Henderson, C. P. Hale, J. R. Magee, M. J. Kavaya, and R. M. Huffaker, "Eyesafe coherent laser radar system at $2.1 \mu\text{m}$ using Tm, Ho:YAG lasers," *Opt. Lett.* (to be published).
6. K. P. Chan, D. K. Killinger, and N. Sugimoto, "Heterodyne doppler $1 \mu\text{m}$ lidar measurement of reduced effective telescope aperture due to atmospheric turbulence," *Appl. Opt.* **30**, 2617-2627 (1991).
7. J. W. Strohbehn, ed., *Laser Beam Propagation in the Atmosphere* (Springer, New York, 1978), and references therein.
8. D. L. Fried, "Optical heterodyne detection of an atmospherically distorted signal wave front," *Proc. IEEE* **55**, 57-67 (1967).
9. S. F. Clifford and S. Wandzura, "Monostatic heterodyne lidar performance: the effect of the turbulent atmosphere," *Appl. Opt.* **20**, 514-516 (1981); erratum **20**, 1502 (1981).
10. J. H. Shapiro, B. A. Capron, and R. C. Harney, "Imaging and target detection with a heterodyne-reception optical radar," *Appl. Opt.* **20**, 3292-3313 (1981).
11. V. I. Tatarski, *The Effects of the Turbulent Atmosphere on Wave Propagation*, IPST Catalog 5319 (National Technical Information Service, Springfield, Va. 1971).
12. P. A. Pincus, M. E. Fossey, J. Holmes, and J. R. Kerr, "Speckle propagation through turbulence: experimental," *J. Opt. Soc. Am.* **68**, 760-762 (1978).
13. J. H. Churnside, R. J. Hill, G. Conforti, and A. Consortini,

- "Aperture size and bandwidth requirements for measuring strong scintillation in the atmosphere," *Appl. Opt.* **28**, 4126-4132 (1989).
14. K. P. Chan and D. K. Killinger, "Enhanced detection of atmospheric-turbulence-distorted 1- μ m coherent lidar returns using a two-dimensional heterodyne detector array," *Opt. Lett.* **12**, 1219-1221 (1991).
 15. J. W. Goodman, "Statistical properties of laser speckle patterns," in *Laser Speckle and Related Phenomena*, J. C. Dainty, ed. (Springer, New York, 1975), chap. 2, pp. 9-75.
 16. M. H. Lee, J. F. Holmes, and J. R. Kerr, "Statistics of speckle propagating through the turbulent atmosphere," *J. Opt. Soc. Am.* **66**, 1164-1172 (1976).
 17. J. F. Holmes, M. H. Lee, and J. R. Kerr, "Effect of the log-amplitude covariance function on the statistics of speckle propagation through the turbulent atmosphere," *J. Opt. Soc. Am.* **70**, 335-360 (1980).
 18. R. H. Kingston, *Detection of Optical and Infrared Radiation* (Springer, New York, 1978).